AN ANALYSIS OF THE KINETICS OF MICROSTRUCTURAL EVOLUTION DURING THE LATE STAGES OF POWDER PROCESSING

BY

SUN MOO HER

A DISSERTATION PRESENTED TO THE GRADUATE SCHOOL
OF THE UNIVERSITY OF FLORIDA IN PARTIAL
FULFILLMENT OF THE REQUIREMENTS
FOR THE DEGREE OF DOCTOR OF PHILOSOPHY

UNIVERSITY OF FLORIDA

1986

Dedicated

To My Leader,

Dr. Robert Thomas DeHoff

ACKNOWLEDGEMENTS

The ideas and logical developments described here are basically originated by Dr. R. T. DeHoff, the chairman of my advisory committee. I am very grateful for the opportunity to work for him.

Many thanks should be given to the late Dr. F. N. Rhines, who passed away during preparation of this dissertation; Dr. G. J. Abbaschian, Dr. E. D. Whitney, Dr. R. W. Gould, all the other professors of the Department of Materials Science and Engineering; and Dr. R. L. Scheaffer of the Department of Statistics for guidance, advice and encouragement.

I am further grateful that this opportunity to pursue my graduate studies was provided by my leaders including Dr. S. J. Kim, Mr. P. K. Hong, Dr. J. O. Seo, Mr. D. H. Park, Dr. H. W. Hwang, Dr. C. J. Yang and Dr. J. Heo.

This research was supported in part by the Army Research Office under contract no. DAAG 29-82-K-0038, and in part from the Department of Materials Science and Engineering through the Microstructures Center of Excellence. I appreciate these contributions.

Mr. S. D. Vora helped me to acquire some of the basic experimental techniques. Mr. Rudy Strohschein, Jr., of the Department of Chemistry assisted me beyond the scope of his duty in the fabrication of sintering apparatus. Mr. T. Gassett helped me by making monetary resources available for this research. I express thanks for all of these.

Mrs. Gail Keim saved me a great deal of time in the preparation of this dissertation by her excellent typing.

H. J. Park HER did not spare her sacrificial assistance during the performance of this work.

TABLE OF CONTENTS

Page

ACKNOWLEDGEMENTS....................iii

LIST OF TABLES....................viii

LIST OF FIGURES....................x

ABSTRACT....................xv

CHAPTER

1 INTRODUCTION....................1

1.1 Sintering as a Microstructural Evolution in Three Dimensional Space....................2
1.2 Three Stages of Sintering....................2
1.3 Purpose of the Present Study....................2

2 MICROSTRUCTURAL EVOLUTION DURING SINTERING....................5

2.1 Introduction....................5
2.2 The Microstructural State....................5
2.2.1 The qualitative microstructural state....................5
2.2.2 The quantitative microstructural state....................6
2.2.3 The topographic microstructural state....................6
2.3 Theory of Microstructural Evolution....................9
2.3.1 The path of microstructural change....................9
2.3.2 The kinematics of microstructural evolution....................9
2.3.2.1 Displacement equations for moving interfaces....................11
2.3.2.2 Interface velocity averages....................13
2.3.3 The kinetics of microstructural evolution....................15
2.4 A Geometrically General Kinetic Theory of the Sintering Process....................17
2.4.1 Introduction....................17
2.4.2 The elements of the cell model....................18
2.4.2.1 The structure, property and evolution of a cell....................18
2.4.2.2 Densification and vacancy annihilation....................22
2.4.2.3 Densification and diffusion fluxes....................24
2.4.3 Densification rate....................29

2.4.4 Vacancy concentration gradients......................30
2.4.4.1 The average vacancy concentration gradients..30
2.4.4.2 Vacancy diffusivities........................31

3 EXPERIMENTAL PROCEDURE..35

3.1 Introduction...35
3.2 Sample Preparation...35
3.2.1 Presintered samples..35
3.2.1.1 Presintered samples for stereological measurements..........................38
3.2.1.2 Presintered samples for the in-situ measurement of shrinkage.................38
3.2.2 A series of sintered samples for stereological characterization.................................38
3.3 Characterization of the Sample...............................40
3.3.1 Density..40
3.3.2 Metric properties..42
3.3.2.1 Polishing procedure..........................43
3.3.2.2 Group one measurements (V_V^P, S_V^{sp}, and M_V^{sp})..43
3.3.2.3 Group two measurements (S_V^{ss}, S_V^{cell}, and L_V^{ssp})..44
3.3.3 Topological properties.....................................46
3.3.3.1 Serial sectioning.............................46
3.3.3.2 Topological analysis.........................49
3.3.4 Metric properties on intermediate serial sections.....57
3.4 In-situ Measurements of Shrinkage............................59
3.4.1 Introduction...59
3.4.2 Monitoring the in-situ dimensional change.............59

4 EXPERIMENTAL RESULTS...62

4.1 Introduction...62
4.2 Microstructures..63
4.3 Paths of Microstructural Evolution...........................63
4.4 Topological Properties.......................................63
4.5 Path Information Obtained from Intermediate Serial Sections..95
4.6 Kinematics...99
4.7 Kinetics..104

5 DISCUSSION...108

5.1 Introduction..108
5.2 Distribution of Local Interface Velocities..................109
5.3 Vacancy Concentration Gradients.............................113
5.3.1 Kinetic considerations....................................114
5.3.1.1 The densification rate......................114
5.3.1.2 The efficiency factor.......................117
5.3.1.3 The parameter y.............................120
5.3.1.4 Average vacancy concentration gradient by kinetic considerations.....................121

5.3.2 Thermodynamic considerations........................123
5.3.2.1 The average vacancy concentration gradient from thermodynamic considerations..123
5.3.2.2 The vacancy concentration of bulk material..125
5.3.2.3 The mean curvature of pore solid interface..126
5.3.2.4 Mean diffusion distance for the annihilation of a vacancy..................127
5.3.2.5 Thermodynamic average vacancy concentration gradient.....................130
5.3.3 The comparison of average vacancy concentration gradients by two independent considerations..........130
5.4 Description of Behavior of Vacancy Annihilation............134
5.5 Generality of the Cell Model and Speculations for Further Studies.......................................138
5.5.1 A test on an intermediate section of the specimen during serial sectioning analysis...........139
5.5.2 Cold pressing and sintering in the late stages of sintering..139
5.5.3 Hot pressing in the late stages of sintering.........144
5.5.4 Loose stack sintering in the intermediate stage of sintering..144

6 CONCLUSIONS...154

6.1 Introduction...154
6.2 Conclusions..154
6.3 Suggestions for Further Study..............................155

REFERENCES..157

BIOGRAPHICAL SKETCH...160

LIST OF TABLES

Table Page

1 The qualitative microstructural state for the porous sintered structure of a pure solid..........................7

2 The quantitative microstructural state of the porous sintered structure of a pure solid..........................8

3 Sources of information for factors required to estimate vacancy concentration gradients by kinetic considerations...32

4 Characteristics of INCO type 123 nickel powder..............37

5 Fundamental relationships of quantitative stereology........41

6 Events that may occur during a serial sectioning analysis and contributions to topological properties........52

7 Metric properties for INCO 123 nickel powder loose stack sintered at 1250°C in H_2..............................71

8 Topological properties of INCO 123 nickel powder loose stack sintered at 1250°C in H_2.......................77

9 Measurements of in-situ kinetics of INCO 123 nickel powder loose stack sintered at 1250°C......................107

10 Kinematics of the microstructural evolution of INCO 123 nickel powder loose stack sintered at 1250°C...........111

11 Densification rate in terms of in-situ kinetics............115

12 Estimation of efficiency factor and y......................118

13 Constants about nickel.....................................122

14 Mean curvature and mean diffusion distance for the annihilation of a vacancy.................................129

15 Comparisons of average vacancy concentration gradients over pore-solid interfacial area.................132

16 Behaviors of vacancy annihilation during sintering 5.5 micron nickel powders at 1250°C........................135

17 Data for analysis of the general kinetic theory for INCO 123 nickel powder cold pressed (25000 psi) and sintered at 1250°C in H_2..................................141

18 The results of analysis of the general kinetic theory for INCO 123 nickel powder cold pressed (25000 psi) and sintered at 1250°C in H_2...................142

19 Data for analysis of the general kinetic theory for INCO 123 nickel powder hot pressed (2000 psi) at 1250°C in vacuum..145

20 The results of analysis of the general kinetic theory for INCO 123 nickel powder hot pressed (2000 psi) at 1250°C in vacuum.............................146

21 Data for analysis of the general kinetic theory for 48 micron pure LINDE spherical copper powder loose stack sintered at 1000°C under H2.........................149

22 Constants about copper.....................................150

23 The results of analysis of the general kinetic theory for 48 micron pure LINDE spherical copper powder loose stack sintered at 1000°C under H_2.........................151

LIST OF FIGURES

Figures Page

1 Illustration of a quantitative microstructural state (P) and a path (A) for a microstructural evolution in (V_V^P, S_V^{SP}, M_V^{SP}) space....10

2 The expansion of a volume by the motion of its bounding surface (a) produces changes in the local geometry of the surface (b)....12

3 The cell construction, showing a grain and its associated porosity, at each stage of sintering....19

4 The bipyramid construction associated with each face in the cell structure....21

5 Area elements, concentration gradients and fluxes associated with diffusional flows in sintering....26

6 INCO 123 nickel powder used in the present investigation....36

7 A boat set-up for the fabrication of the presintered specimen used for in-situ shrinkage measurement....39

8 Measurement of a cell boundary area and grain boundary area....45

9 The relationship between decrease in the depth of the microhardness indentation and decrease in the length of diagonals of the indentation....48

10 Basic idea for the estimation of G^{max}, G^{min} and N^{iso}....50

11 Schematic of a serial sectioning analysis of the sample in Figure 10....53

12 Schematic of the topological analysis of the sample in Figure 10....55

13 Distinguishing between a connected pore (C) and an isolated pore (I)....58

14 The set-up for monitoring in-situ dimensional change during sintering....60

15 Photomicrographs of INCO 123 nickel powder loose stack sintered at 1250°C to $V_V^S = 0.890$ (a) unetched (X200) and (b) etched (X500)....64

16 Photomicrographs of INCO 123 nickel powder loose stack sintered at 1250°C to $V_V^S = 0.914$ (a) unetched (X200) and (b) etched (X500)....65

17 Photomicrographs of INCO 123 nickel powder loose stack sintered at 1250°C to $V_V^S = 0.935$ (a) unetched (X200) and (b) etched (X500)....66

18 Photomicrographs of INCO 123 nickel powder loose stack sintered at 1250°C to $V_V^S = 0.946$ (a) unetched (X200) and (b) etched (X500)....67

19 Photomicrographs of INCO 123 nickel powder loose stack sintered at 1250°C to $V_V^S = 0.957$ (a) unetched (X200) and (b) etched (X500)....68

20 Photomicrographs of INCO 123 nickel powder loose stack sintered at 1250°C to $V_V^S = 0.968$ (a) unetched (X200) and (b) etched (X500)....69

21 Photomicrographs of INCO 123 nickel powder loose stack sintered at 1250°C to $V_V^S = 0.974$ (a) unetched (X200) and (b) etched (X500)....70

22 Path of microstructural change for the pore-solid interface....72

23 Path of microstructural change for the integral mean curvature per unit volume of the pore-solid interface....73

24 Variations of the surface area and the cell boundary area per unit volume of the grain boundary network with volume fraction of the solid phase....74

25 Path of microstructural change of the length per unit volume of triple lines formed by the intersection of grain boundaries with the pore-solid interface....75

26 Dependence of maximum connectivity on the volume fraction of solid during loose stack sintering of INCO 123 nickel powder at 1250°C....78

27 Dependence of minimum connectivity on the volume fraction of solid during loose stack sintering of INCO 123 nickel powder at 1250°C....79

28 Variation of the number of isolated pores per unit volume with the volume fraction of solid during loose stack sintering of nickel at 1250°C........................80

29 Variation of connectivities with volume analyzed for 5.5 micron nickel powder loose stack sintered to $V_V^S = 0.890$..81

30 Variation of connectivities with volume analyzed for 5.5 micron nickel powder loose stack sintered to $V_V^S = 0.914$..82

31 Variation of connectivities with volume analyzed for 5.5 micron nickel powder loose stack sintered to $V_V^S = 0.935$..83

32 Variation of connectivities with volume analyzed for 5.5 micron nickel powder loose stack sintered to $V_V^S = 0.946$..84

33 Variation of connectivities with volume analyzed for 5.5 micron nickel powder loose stack sintered to $V_V^S = 0.957$..85

34 Variation of connectivities with volume analyzed for 5.5 micron nickel powder loose stack sintered to $V_V^S = 0.968$..86

35 Variation of connectivities with volume analyzed for 5.5 micron nickel powder loose stack sintered to $V_V^S = 0.974$..87

36 Variation of number of separate parts with volume analyzed for 5.5 micron nickel powder loose stack sintered to $V_V^S = 0.890$....................................88

37 Variation of number of separate parts with volume analyzed for 5.5 micron nickel powder loose stack sintered to $V_V^S = 0.914$....................................89

38 Variation of number of separate parts with volume analyzed for 5.5 micron nickel powder loose stack sintered to $V_V^S = 0.935$....................................90

39 Variation of number of separate parts with volume analyzed for 5.5 micron nickel powder loose stack sintered to $V_V^S = 0.946$....................................91

40 Variation of number of separate parts with volume analyzed for 5.5 micron nickel powder loose stack sintered to $V_V^S = 0.957$....................................92

41 Variation of number of separate parts with volume analyzed for 5.5 micron nickel powder loose stack sintered to $V_V^S = 0.968$....................................93

42 Variation of number of separate parts with volume analyzed for 5.5 micron nickel powder loose stack sintered to $V_V^S = 0.974$....................................94

43 Dependence of the metallographically determined volume fraction of connected porosity and isolated porosity on the volume fraction of porosity................96

44 Dependence of surface area of the connected porosity per unit volume on the volume fraction of solid during loose stack sintering of nickel at 1250°C...........97

45 Dependence of integral mean curvature of the connected porosity on the volume fraction of solid during loose stack sintering of nickel at 1250°C........................98

46 Dependence of volume fraction of pore (metallographic) on the logarithm of sintering time........................101

47 Dependence of surface area per unit volume on the logarithm of sintering time..............................102

48 Dependence of integral mean curvature per unit volume on the logarithm of sintering time........................103

49 Photographs of in-situ specimen of 5.5 micron nickel powder during loose stack sintering at 1250°C at several sintering times..105

50 Dependence of volume fraction of pore on the logarithms of sintering time for a continuous sintering and a discontinuous sintering.................................106

51 Comparison of surface average velocity, $\overline{v}_S$, mean curvature average velocity, $\overline{v}_M$, and Gaussian curvature average velocity, $\overline{v}_K$, during loose stack sintering 5.5 micron nickel powder at 1250°C...........................110

52 Densification rate in terms of a continuous change of volume of pore per mole of nickel per sec versus volume fraction of solid for loose stack sintered 5.5 micron nickel powder at 1250°C.................................116

53 Variation of the efficiency factor, $\overline{f}$, and rough estimation of $\overline{f}[1/(1-V_V^P)]$ with volume fraction of the solid phase...119

54 Average vacancy concentration gradients by capillarity theory....124

55 Variation of the mean curvature of isolated pores, connected pores and total pores with volume fraction of solid....128

56 Variation of average distances for the annihilation of a vacancy with the volume fraction of solid....131

57 Comparison of variations of average vacancy concentration gradients over pore-solid interface area by kinetic considerations and those by thermodynamic considerations with the volume fraction of solid for 5.5 micron nickel powder loose stack sintered at 1250°C....133

58 Dependence of average vacancy annihilation rate on the volume fraction of solid for 5.5 micron nickel powder loose stack sintered at 1250°C....136

59 Variations of average time required for monolayer of vacancy to annihilate with volume fraction of solid for 5.5 micron nickel powder loose stack sintered at 1250°C....137

60 Comparison of variations of average vacancy concentration gradients over pore-solid interface area by two independent considerations with volume fraction of solid at a random section (no. 6) during the serial sectioning analysis of 5.5 micron nickel powder loose stack sintered at 1250°C....140

61 Comparison of variations of average vacancy concentration gradients over pore-solid interface by two independent considerations with the volume fraction of solid for 5.5 micron nickel powder cold pressed (25000 psi) and sintered at 1250°C in H_2....143

62 Comparison of variations of average vacancy concentration gradients over pore-solid interface by two independent considerations with the volume fraction of solid for 5.5 micron nickel powder hot pressed (2000 psi) at 1250°C in vacuum....147

63 Comparison of variations of average vacancy concentration gradients over pore-solid interface by two independent considerations with the volume fraction of solid for 48 micron pure LINDE spherical copper powder loose stack sintered at 1000°C±5°C under H_2....152

Abstract of Dissertation Presented to the Graduate School of
the University of Florida in Partial Fulfillment of the
Requirements for the Degree of Doctor of Philosophy

AN ANALYSIS OF THE KINETICS OF MICROSTRUCTURAL EVOLUTION DURING THE LATE STAGES OF POWDER PROCESSING

By

Sun Moo Her

December 1986

Chairman: Dr. R. T. DeHoff
Major Department: Materials Science and Engineering

A geometrically general kinetic theory of microstructural evolution in sintering has been developed, based on two alternate space-filling constructs: cells associated with the grains in the system and bipyramids associated with the cell faces. The theory connects the evolution of global geometric properties with specifically defined averages of diffusion fluxes, or equivalently, concentration gradients in the system.

This theory has been tested experimentally by combining stereological measurements of the quantitative path of microstructural change with observations of the kinetics of shrinkage.

Calculated values of the average vacancy concentration gradient on the pore surface are shown to be in excellent agreement with independent estimates of these gradients.

CHAPTER 1
INTRODUCTION

1.1 Sintering as a Microstructural Evolution in Three Dimensional Space

Powder processing has become a commonplace technology in the production of materials. Some materials can only be made by starting with a powder mixture; in other cases, powder processing has been shown to have economic or other overriding advantages that warrant its use.

The traditional approach to the investigation of the nature of sintering has been to measure the time-temperature function of some simple dimensional change, such as the change in weld neck diameter.[1-8] Then, assuming that this is representative of the changes which constitute sintering, a mechanism of material transport is inferred for the sintering process. However, this kind of approach has yielded no principles which can be used to predict either the geometric path of sintering or the rate of progress in the microstructural evolution in real, three dimensional aggregates of powder particles.

A new general approach to the description of microstructural evolution has recently been presented.[9] This theory evolved from application of topology and stereology to the study of microstructural evolution during powder processing.[10-15] The concepts and techniques developed in this approach form the fundamental basis of this study.

1.2 Three Stages of Sintering

The sequence of microstructural states[10,16,17] traversed by a porous structure as it sinters may be conveniently divided into three stages:

First stage:	connectivity of the aggregate increases as shrinkage brings into contact particles that were not previously touching. During this stage, a single crystal particle in contact cannot undergo grain growth, but neck growth occurs.
Second stage:	connectivity of the pore network decreases to zero. Geometrically the dominant process is channel closure; redundant connections are eliminated gradually.
Third stage:	isolated pores are formed by disconnecting the pore network. Isolated pores shrink toward zero volume as densification proceeds.

The third stage is a primary focus in this study because it is of considerable commercial and scientific interest.

1.3 Purpose of the Present Study

During the past three decades, most of the innovations[11,13,15,18-22] accomplished in expanding the understanding of the nature of sintering have been limited to the establishment of concepts and measurement of parameters associated with characterization of microstructural state during microstructural evolution. Concepts[12,13] associated with kinematics of microstructural evolution during powder processing are also well established, but no systematic experimental evaluation of the kinematics has emerged. Furthermore, kinetic studies[13,14,23,24] are on the stage of the evolution of the theories.

The kinetics of microstructural evolution embodies a description of the rate of traverse of the path in terms of the physical phenomena that produce the change. This requires a formulation of the driving forces that cause the observed state changes, the flows that these driving forces produce, and the establishment of the connection between these flows and the resulting changes in the geometry of the microstructure.

A geometrically general kinetic theory[24] has recently been developed on the basis of a cell model. This is a significant beginning in the development of a general theory of microstructural evolution.

The primary objective of this research was to test the validity of this new born geometrically general kinetic theory by the use of precise kinetic measurements and path information which were obtained through both metric and topological characterization of microstructural evolution during the late stages of loose stack sintering. Connections between the kinematics evaluated through both metric and topological characterizations of microstructural evolution and the kinetic theory constitute a secondary objective of this research.

In order to accomplish these objectives, all of the previously developed concepts and experimental techniques were employed. In-situ measurements of shrinkage of sintered powder samples were carried out to complete the quantitative kinetic information.

Theories of microstructural evolution during sintering are reviewed in Chapter 2, where the focus is on the geometrically general kinetic theory. This review is followed by description of the experimental procedure in Chapter 3 and experimental results in Chapter 4. Finally, a test of the cell model based on experiments, literature and inferences is followed by speculation about the general applicability of the model.

CHAPTER 2
MICROSTRUCTURAL EVOLUTION DURING SINTERING

2.1 Introduction

The elements of a theory of microstructural evolution consist of three parts: 1) the stereological measures which permit the quantitative characterization of the microstructural state; 2) the interface displacement equations, which relate the rate of change of global geometric properties of evolving feature sets to the distribution of local interface velocities; and 3) kinetic models that establish the connection between the local interface velocity distribution and the mass transport which produces the local interface displacements.

2.2 The Microstructural State

The geometric state of a microstructure may be characterized at three different levels[11] of increasing complexity.

2.2.1 The qualitative microstructural state

From a geometric point of view, microstructures consist of zero-, one-, two- and three-dimensional features (points, lines, interfaces and volumes). Although there are exceptions,[*] in most cases these features result from the incidence of cells[25] (grains or particles) upon each other. Two cells meet at an interface, three meet at a triple line, and four define a quadruple point.

---

[*] Dislocations and stacking faults

The qualitative microstructural state is a complete list of the kinds of features that exist in the system. Table 1 provides an exhaustive list of the features that may be encountered in the porous sintered structure of a pure solid. Sections of cells, interfaces and triple lines appear as areas, boundaries and triple points on the two-dimensional image in the microscope. Quadruple points are not observable on sections, but must be inferred from the other features that exist.

2.2.2 The quantitative microstructural state

The quantitative microstructural state is obtained by evaluating geometric properties displayed in Table 1. The list of geometric properties provided in Table 2 is not exhaustive, but exhibits the geometric properties that are potentially most useful in describing the microstructural state of the porous sintered body of a pure solid. This list of geometric properties is crucial in the characterization of the quantitative microstructural state because all of the properties have unambiguous meaning for structures of arbitrary complexity and are accessible to stereological estimation. These properties play the central role in the interface displacement equations in the kinematics of microstructural evolution.

2.2.3 The topographic microstructural state

The topographic microstructural state reports nonuniformities[25] in the microstructure including anisotropy, gradients, and tendencies for features to positively or negatively associate with one another.

Table 1
The qualitative microstructural state for
the porous sintered structure of a pure solid

Dimension	Feature	Designation*
3	Volumes	s, p
2	Interfaces	ss, sp
1	Triple lines	sss, ssp
0	Quadruple points	ssss, sssp

* s : solid p : pore

Table 2
The quantitative microstructural state of the porous sintered microstructure of a pure solid

Symbol	Property
V_V^s	Volume fraction of solid
V_V^p	Volume fraction of porosity
S_V^{ss}	Surface area of grain boundaries per unit volume
S_V^{sp}	Area of solid-pore interface per unit volume
M_V^{sp}	Integral mean curvature of solid-pore interface per unit volume
L_V^{sss}	Length of grain edges per unit volume
L_V^{ssp}	Length of intersection lines of solid-pore interface and grain boundaries per unit volume
N_V^{iso}	Number of isolated pores per unit volume
G_V	Connectivity of the sintered solid body per unit volume

2.3 Theory of Microstructural Evolution

The evolution of microstructure during sintering may be formulated at three levels of understanding.

2.3.1 The path of microstructural change

The path of microstructural change[18] is the sequence of microstructural states through which the system passes during a process. The microstructural state of a system, as illustrated in Figure 1, may be thought of as a point in space which has a number of dimensions equal to the number of variables quantified in identifying the state. The path, as illustrated in Figure 1, is then the one-dimensional curve in that space which connects the points in the sequence of states that characterizes the process. In practice, the path is represented by a collection of plots of the variables measured versus one geometric property that has been chosen to report the overall extent of the process. The determination of the path frequently provides insights into the nature of the process[18] that are not easily accessible from kinematic or kinetic observations, because the path focuses purely on geometric relationships in the process.

2.3.2 The kinematics of microstructural evolution

Motions of geometric features produce changes in the geometric properties associated with these features. The growth (or shrinkage) of any feature is best visualized and described in terms of the motion of its boundary. Thus, the growth (or shrinkage) of features of the p (pore) phase is formulated in terms of displacements of the sp (solid-pore) interface.

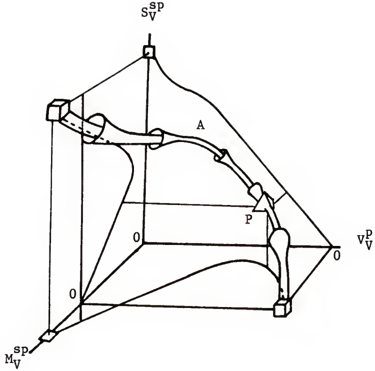

Figure 1. Illustration of a quantitative microstructural state (P) and a path (A) of microstructural evolution in $(V_V^P, S_V^{sp}, M_V^{sp})$ space.

2.3.2.1 Displacement equations for moving interfaces

Consider a closed sp interface bounding a p feature, in Figure 2. In some time interval, dt, this interface moves to a new configuration and position. In the general case, some elements of the interface may be displaced toward the p phase, and some away from it. Let it be assumed that this closed surface is everywhere smooth and continuous; i.e. it has no sharp ridges or cusps. This assumption is necessary so that each element of surface on the original interface can be unambiguously associated with an element on the displaced surface. This one-to-one association is accomplished by constructing normals to the original surface and considering the point of intersection of the normal with the new surface as the corresponding point. The local displacement of the surface may then be defined as the distance between corresponding points along the normal, dn. The local velocity of the interface is then defined by

$$v \equiv \frac{dn}{dt} \tag{1}$$

This velocity has, for any given process, some distribution of values upon the surface, and some average value. Rates of change of all of the metric properties associated with the interface are related to this velocity distribution. It can be shown that[12]

$$\frac{dV_V^p}{dt} = \iint_{S_V^{sp}} v\,dS \tag{2}$$

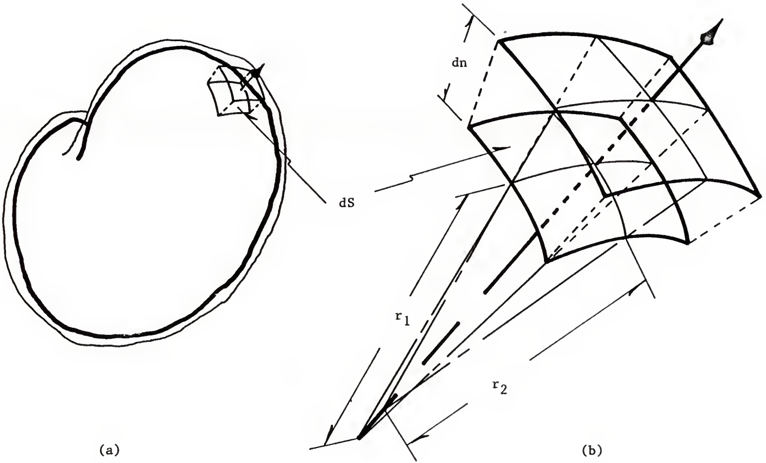

Figure 2. The expansion of a volume by the motion of its bounding surface (a) produces changes in the local geometry of the surface (b).
$H \equiv \frac{1}{2}(\frac{1}{r_1}+\frac{1}{r_2})$, $K \equiv \frac{1}{r_1} \cdot \frac{1}{r_2}$.

$$\frac{dS_V^{sp}}{dt} = 2 \iint_{S_V^{sp}} vHdS = 2 \iint_{M_V^{sp}} vdM \qquad (3)$$

$$\frac{dM_V^{sp}}{dt} = \iint_{S_V^{sp}} vKdS = \iint_{\Omega_V} vd\Omega \qquad (4)$$

where dS is the element of surface area in Figure 2, H and K are local values of the curvature functions defined as $H = 1/2(\kappa_1 + \kappa_2)$ (local mean curvature) and $K = \kappa_1 \cdot \kappa_2$ (the Gaussian curvature) where $\kappa_1 = 1/r_1$, $\kappa_2 = 1/r_2$. The part of the total value of M for the surface associated with the area element dS is $dM = HdS$; $d\Omega = KdS$ is the spherical image (solid angle subtended by the normals) at dS. These are the basic equations relating the total properties of a moving interface to the distribution of velocities on the interface.

If the interface has singularities, sharp ridges or cusps (e.g., triple lines or quadruple points), then the one-to-one mapping of the initial and displaced interface may break down in the vicinity of these discontinuities. Equations (2)-(4) are not valid in these regions. The errors introduced are of second order in equation (2), and may be neglected; however, the effects upon the validity of equations (3) and (4) are now under investigation.[26]

2.3.2.2 Interface velocity averages

Since the interface velocity has some distribution of values from point-to-point over the surface and has some average value, three average interface velocities may be defined, each weighted differently. These are derived from the rates of change of the three fundamental metric[13] properties associated with the surface. These three average interface velocities may be obtained from the interface displacement equations, by multiplying numerator and denominator of the right hand sides by $\iint_{S_V^{sp}} dS$, $\iint_{S_V^{sp}} HdS$, $\iint_{S_V^{sp}} KdS$, respectively. Recall that

$$M_V \equiv \iint_{S_V^{sp}} HdS \tag{5}$$

and

$$\iint_{S_V^{sp}} KdS = 4\pi(N_V - G_V) \tag{6}$$

provided the surface is smooth and closed. Then one may define

$$\bar{v}_S \equiv \frac{\iint vdS}{\iint dS} = \frac{1}{S_V^{sp}} \frac{dV_V^p}{dt} \tag{7}$$

$$\bar{v}_H \equiv \frac{\iint vHdS}{\iint HdS} = \frac{1}{2M_V^{sp}} \frac{dS_V^{sp}}{dt} \tag{8}$$

$$\bar{v}_K \equiv \frac{\iint vKdS}{\iint KdS} = \frac{1}{4\pi(N_V - G_V)} \frac{dM_V^{sp}}{dt} \tag{9}$$

The comparison of these various averages can provide qualitative insight into the distribution of interface velocities in the system. For example,[27] consider an aggregate of growing platelets in which the rate of thickening is small, while the edgewise growth rate is high. The surface area average velocity $\bar{v}_S$ will report a small average velocity, because most of the interface (the platelet faces) is moving with a small velocity. In the same system, $\bar{v}_H$ will be much larger, because the slow moving regions of the interface contribute very little to the total curvature, while the platelet edges, which are highly curved, contribute most to M_V. These definitions and relations are applied to the analysis of the kinetics.

2.3.3 The kinetics of microstructural evolution

The kinetics of microstructural evolution connects the path and kinematics with the physics of the process. The transition from kinematics to kinetics is accomplished by expressing the local interface velocity, v, in terms of the physical mechanisms that operate. In order to do this, a controlling mechanism is assumed and an expression for v at a position on the interface is derived. This expression is generally obtained by analyzing a local mass (or in some cases, energy) balance at the interface. The resulting equation usually takes the form of an interface accommodation equation. What must be accommodated is a change in concentration (or a change in energy) as the boundary moves.

For control of the moving interface by the rate of an interface reaction, it is found that[23]

$$v = k(H - H_0) \tag{10}$$

where k is a combination of an interface reaction rate constant and thermodynamic factors related to capillary effects, H is the local mean surface curvature, and H_0 is an effective mean curvature value that corresponds to the concentration in the matrix phase.

For control by surface diffusion,[14] the local mass balance gives

$$v = \frac{kD_S b}{\Delta C} \nabla^2 H \qquad (11)$$

where D_S is an interfacial diffusion coefficients, k involves thermodynamic quantities in capillarity theory, ΔC is the concentration difference across the interface, b is the effective thickness of the interface layer, and $\nabla^2 H$ is the Laplacian of the local mean curvature on the surface.

For control by volume diffusion, in the matrix phase the mass balance gives

$$v = \frac{D}{\Delta C} \vec{\nabla} C_S \qquad (12)$$

where ΔC is the concentration differences across the interface, D is the volume diffusion coefficient in the matrix, and $\vec{\nabla} C_S$ is the concentration gradient in the matrix evaluated at the moving interface.

Insertion of these equations into the kinematic equations permits a prediction of the time variation of the global properties V_V, S_V and M_V, which are stereologically accessible. For example, for control by volume diffusion insertion of equation (12) into equations (2), (3) and (4) yields

$$\frac{dV_V}{dt} = \frac{D}{\Delta C} \langle \vec{\nabla} C_S \rangle \cdot S_V \qquad (13)$$

$$\frac{dS_V}{dt} = \frac{2D}{\Delta C} \langle \vec{\nabla} C_M \rangle \cdot M_V \qquad (14)$$

$$\frac{dM_V}{dt} = \frac{D}{\Delta C} \langle \vec{\nabla} C_\Omega \rangle \cdot \Omega_V \qquad (15)$$

where $\langle \vec{\nabla} C_S \rangle \equiv \iint_S \vec{\nabla} C dS / \iint dS$, the concentration gradient averaged over surface area, $\langle \vec{\nabla} C_M \rangle \equiv \iint_M \vec{\nabla} C dM / \iint dM$, the concentration gradient averaged over the integral mean curvature, and $\langle \vec{\nabla} C_\Omega \rangle \equiv \iint_\Omega \vec{\nabla} C d\Omega / \iint d\Omega$, the concentration gradient averaged over the spherical image.

2.4 A Geometrically General Kinetic Theory of the Sintering Process

2.4.1 Introduction

A geometrically general kinetic theory[24] of microstructural evolution during sintering has been developed recently based on two alternate space-filling constructs: cells associated with the grains in the system and bipyramids associated with cell faces. It is distinguished from existing descriptions[1-8] primarily in its attempt to maintain geometric and mechanistic rigor. The model connects the evolution of global geometric properties with specifically defined averages of diffusion fluxes, or, equivalently, concentration gradients in the system. The approach permits significant penetration of the problem of the description of sintering without important simplifying assumptions.

The elements of the cell model[24] are described in this section and together with the strategies used to relate the model with an experimental demonstration.

2.4.2 The elements of the cell model[24]

2.4.2.1 The structure, property and evolution of a cell

At any instant of observation a partially sintered structure consists of a pore phase, which may be wholly or partially connected or disconnected, and a solid phase, which contains a grain boundary network that may be disconnected, partially connected, or completely connected. A space filling cell structure may be visualized for such a system such that 1) each cell contains one grain in the polycrystalline structure; and 2) each cell also contains the porosity that is associated with that grain. The space filling cell, as illustrated in Figure 3, has a surface that is partially occupied by grain boundary facets and partially by porosity. Unambiguous construction of individual cells requires the assumption that the grain boundaries are planar. This assumption is reasonably valid for the first stage when the grain boundary network is disconnected and is not expected to be a serious approximation even in the late stages of sintering. Each cell in the structure is thus a polyhedron with flat sides. The jth face of any cell, as illustrated in Figure 4, is associated with the two cells, labelled 1 and 2, and a pyramid in each cell, thus two pyramids, a bipyramid j. The jth bipyramid has a face area A_j and pedal functions[**] P_{1j} and and P_{2j}; the volume of the bipyramid is

$$V_j = 1/3\ A_j[P_{1j} + P_{2j}] \qquad (16)$$

[**] The perpendicular distance from the centroid of cell i to the jth face, P_{ij} is defined as the pedal function for that face.

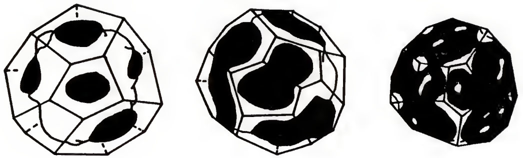

Figure 3. The cell construction, showing a grain and its associated porosity, at each stage of sintering.[24]

Sintering produces microstructural evolution that alters the cell structure. These changes may be described in terms of the motions of the cell boundaries relative to any reference point (centroid of the cell for consistency) within the cell. The change in the volume of the bipyramid in two adjacent cells that are associated with face j is

$$dV_j = A_j[dP_{1j} + dP_{2j}] \tag{17}$$

Motions of faces that result in rotation or expansion contribute higher order differentials to the volume change. Thus equation (17) is a rigorous and complete evaluation of the first order change in the volume of the bipyramid. The change in volume of the system may be obtained by summing over the faces in cells and over all of the cells in a system.

Since the cell faces are generated from the grain boundary network in the system, motion of the cell faces is associated with motion of the grain boundaries relative to the centroid of their cells. The change in the pedal functions, P_{ij} [i=1,2] in equation (16), may be unambiguously divided into two contributions: 1) decrease in P_{ij} due to vacancy annihilation (VA) in the grain boundary, and 2) change in P_{ij} not associated with vacancy annihilation; motions of this type are definied to be grain boundary migration (GBM). Thus, in general,

$$dP_{ij} = (dP_{ij})_{VA} + (dP_{ij})_{GBM} \tag{18}$$
$$(i = \text{cells},\ j = \text{faces})$$

Vacancy annihilation always decreases the pedal function and contributes to densification. Grain boundary migration may increase or decrease the

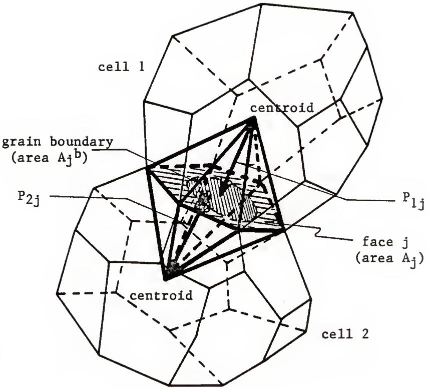

Figure 4. The bipyramid construction associated with each face in the cell structure.

pedal function and does not contribute to densification. Vacancy annihilation therefore results in changes in the volume of the bipyramids. On the other hand, grain boundary migration does not result in changes in the volume of the bipyramids, but results in change in the position of the cell faces. The change in volume of a system thus becomes

$$dV = \sum_{j=1}^{F} dV_j = \sum_{j=1}^{F} A_j[(dP_{1j})_{VA} + (dP_{2j})_{VA}] \tag{19}$$

where F is the total number of faces in the system.

2.4.2.2 Densification and vacancy annihilation

The decrease in pedal function that contributed to densification is unambiguously associated with vacancy annihilation at the grain boundary on the bipyramid face. Let the area of grain boundary on face j be A_j^b. This is some fraction of the area of the cell face, A_j. An efficiency factor f_j for face j is defined as

$$f_j \equiv A_j/A_j^b \tag{20}$$

This parameter varies from a very large value at the beginning of sintering when the grain boundary occupies a small fraction of the cell face to 1 in the late stages when faces become completely covered. If the cell boundary network intersects the pore volume randomly, the estimate of average value of f_j, $\bar{f}$ would be $\bar{f} = 1/(1 - V_V{}^P)$ since $\bar{f}_j = 1/(\bar{A}_j^b/\bar{A}_j) = 1/1-V_V^P$. Actually, due to the non-random intersection of the cell boundary with the pore volume for a porous sintered structure, $\bar{f}$ has a larger value than $1/(1-V_V{}^P)$ (Figure 53).

Let $\bar{\dot{n}}_{Aj}$ be the rate of annihilation of vacancies on face j, with units (vacancies per cm^2 sec). Continuity requires that the rate of annihilation of vacancies over a single grain boundary facet will be constant; departures from uniformity will tend to produce stresses that return the local rate to a uniform value. In a time interval, dt, the volume of vacant sites annihilated in face j is $\Omega° \bar{\dot{n}}_{Aj} A_j^b$ dt, where $\Omega°$ is the atomic volume. This volume of lattice sites annihilated corresponds to the removal of a slab of material with cross sectional area A_j^b and thickness $(dP_{1j})_{VA} + (dP_{2j})_{VA}$; i.e.,

$$\Omega° \bar{\dot{n}}_{Aj} A_j^b dt = -A_j^b[(dP_{1j})_{VA} + (dP_{2j})_{VA}] \tag{21}$$

The minus sign comes from the fact that a positive rate of annihilation of vacancies produces a decrease in the pedal function sum. From equations (19), (20) and (21), equation (22) is derived:

$$\frac{dV}{dt} = -\Omega° \bar{f} \bar{\dot{n}}_A A_b \tag{22}$$

where $\bar{f}$ is the average efficiency factor defined by

$$\bar{f} \equiv \frac{\sum_{j=1}^{F} f_j \bar{\dot{n}}_{Aj} A_j^b}{\sum_{j=1}^{F} \bar{\dot{n}}_{Aj} A_j^b} \quad , \tag{23}$$

$\bar{\dot{n}}_A$ is the average rate of annihilation of vacancies in the structure, defined by

$$\bar{\dot{n}} \equiv \frac{\sum_{j=1}^{F} \bar{\dot{n}}_{Aj} A_j^b}{\sum_{j=1}^{F} A_j^b} \tag{24}$$

and A_b is the total grain boundary area in the structure, given by

$$A_b \equiv \sum_{j=1}^{F} A_j^b \tag{25}$$

2.4.2.3 Densification and diffusion fluxes

Vacancies that are annihilated to produce densification in sintering are supplied from the pore-solid interface in the vicinity of the grain boundary upon which they are annihilated. Vacancies may be supplied from the surface through the lattice to the grain boundary, or they may travel in the zone of high diffusivity adjacent to the grain boundary. Some of the vacancies generated at the pore-solid interface may find their way back to that interface at a region of more positive local mean curvature and be removed from the system at a pore surface sink, rather than at a grain boundary. The subset of vacancies that travel from surface source to surface sink aids the surface rounding process, but cannot contribute to densification.

The element of area of the pore-solid interface, $d\vec{S}$, as illustrated in Figure 5, may be represented by a vector that is locally normal to the surface with a magnitude equal to the area of the element. The volume of solid adjacent to the element is assumed to be in local equilibrium with the surface element, and possesses a vacancy concentration, C_V, which is related to the mean curvature of the surface, H. There also exists a vacancy concentration gradient, $\vec{\nabla} C_S$, and a correponding vacancy diffusion flux, $\vec{J}_V$, in this volume element. In time dt, this local flux contributes $\vec{J}_V \cdot d\vec{S}dt$ vacancies into the volume of the solid phase.

The total number of vacancies supplied to the solid phase from all of the pore surface in the system at time dt is

$$dN_V^s = \iint_S \vec{J}_V \cdot d\vec{S}dt \tag{26}$$

If there is negligible accumulation of vacancies within the volume of the solid phase, then those vacancies that enter the system at the pore surface and do not re-emerge at the pore surface must flow to the grain boundaries, where their annihilation produces densification.

Let L be the total length of ssp triple line at any moment in the system. Grain boundary diffusion fluxes into the solid phase originate from surface elements along the ssp triple line. The volume element of solid adjacent to a ssp triple line, in Figure 5, has a vacancy concentration, C_V, generally assumed to be in equilibrium with the element and its curvature, H. This volume element also has a concentration gradient of vacancies, $\vec{\nabla}C$, and corresponding vacancy flux vector, $\vec{J}$.

In time dt, the number of vacancies supplied to the grain boundary from the surface element associated with the ssp triple line segment $d\vec{L}$ is $\vec{J}_b \cdot \hat{n}bdL$, where $\vec{J}_b$ is the grain boundary component of vacancy flux, $\vec{J}$, $\hat{n}$ is a directional vector of the surface element $d\vec{S}_b = \vec{b} x d\vec{L}$, over which the grain boundary component of vacancy flux, $\vec{J}_b$, acts and $\vec{b}$ is a vector normal to the grain boundary and has a magnitude that represents the thickness of the zone of enhanced diffusivity. The total number of

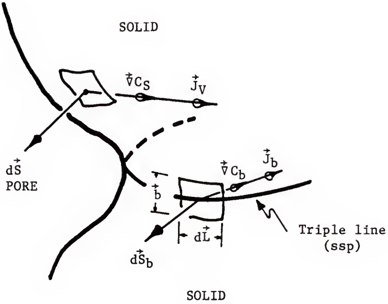

Figure 5. Area elements, concentration gradients and fluxes associated with diffusional flows in sintering.[24]

vacancies supplied to grain boundaries from the surface adjacent to the ssp triple line in time dt is

$$dN_V^b = \int_L \vec{J}_b \cdot \hat{n} b dL dt \tag{27}$$

All of these vacancies move in along the grain boundary where annihilation contributes to densification.

In time dt, the total number of vacancies supplied to grain boundaries from the pore-solid interface, from equations (26) and (27), is

$$dN_V = dN_V^s + dN_V^b = \iint_S \vec{J}_V \cdot d\vec{S} dt + \int_L \vec{J}_b \cdot \hat{n} b dL dt \tag{28}$$

The total number of vacancies annihilated at grain boundaries in the same time interval is

$$dN_V = \overline{\dot{n}}_A A_b dt \tag{29}$$

Under the assumption that the accumulation of vacancies within the volume of the solid phase is negligible in comparison with the flow through the solid, and from equations (22), (28) and (29), the rate of volume shrinkage becomes

$$\frac{dV}{dt} = -\Omega^\circ \overline{f} \overline{\dot{n}}_A A_b = -\Omega^\circ \overline{f} \left[\iint_S \vec{J}_V \cdot d\vec{S} + b \int_L \vec{J}_b \cdot \hat{n} dL \right] \tag{30}$$

Introduce definitions of average lattice flux over the surface $\bar{J}_V$, and average grain boundary flux over ssp triple line, $\bar{J}_b$, and from Fick's Law,

$$\bar{J}_V \equiv \iint_V \vec{J}_V \cdot d\vec{S} \Big/ \iint_S dS = -D_V \langle \vec{\nabla} C_S \rangle \tag{31}$$

and

$$\bar{J}_b \equiv \int \vec{J}_b \cdot \hat{n} dL \Big/ \int_L dL = -D_b \langle \vec{\nabla} C_b \rangle \tag{32}$$

where

$$\langle \vec{\nabla} C_S \rangle \equiv \iint_S \vec{\nabla} C_S \cdot d\vec{S} \Big/ \iint_S dS \tag{33}$$

$$\langle \vec{\nabla} C_b \rangle \equiv \int_L \vec{\nabla} C_b \cdot \hat{n} dL \Big/ \int_L dL \tag{34}$$

and D_V, D_b are vacancy diffusivity in the lattice and grain boundary, respectively. Equation (30) may be written

$$\frac{dV}{dt} = \Omega^\circ \bar{f} [D_V \langle \vec{\nabla} C_S \rangle \cdot S + b \cdot D_b \cdot \langle \vec{\nabla} C_b \rangle \cdot L] \tag{35}$$

or

$$\frac{dV}{dt} = \Omega^\circ \bar{f} D_V \langle \vec{\nabla} C_S \rangle \cdot S^{sp} [1 + y] \tag{36}$$

where

$$y = \frac{bD_b}{D_V} \cdot \frac{L^{ssp}}{S^{sp}} \cdot \frac{\langle \vec{\nabla} C_b \rangle}{\langle \vec{\nabla} C_S \rangle} \tag{37}$$

Inspection of equation (36) suggests that under the assumption of $\langle \vec{\nabla} C_b \rangle / \langle \vec{\nabla} C_S \rangle \approx 1$, values of all parameters except $\langle \vec{\nabla} C_S \rangle$ contained in the equation are accessible to evaluation. The value of $\langle \vec{\nabla} C_S \rangle$ therefore could be evaluated and compared with the value of the same parameter obtained from alternative independent considerations in order to assess the validity of the equation (35). Discussions of the validity of the equation and the cell model are described in Chapter 5. Analysis of equation (36) follows in the next section.

2.4.3 Densification rate

In order to obtain the derivative of volume change of the sintered body with respect to time, it is useful to devise a kinetic law governing the process in the range of interest. In many cases, sintered density or parameter values are obtained as a function of time for a given temperature. An empirical equation relating the volume fraction of porosity (V_V^P) to sintering time (t) (see Figure 49) in the particular range of sintering time involved in this research may be written

$$V_V^P = a \ln t + b \tag{38}$$

where a and b are constants which are determined by the powder and process employed. The derivative of volume change of the sintered body with respect to time is obtained from equation (38),

$$\frac{dV_V^P}{dt} = \frac{a}{t} \tag{39}$$

where a is obtained from the slope of the plot of volume fraction of porosity versus natural logarithm of sintering time.

Measurement of volume fraction of porosity requires the measurement of density. The density of a sintered body may be measured by the water immersion method,[28] which is described in detail in Chapter 3. The density variation may also be measured by monitoring in-situ the dimensional change of the sample. Let ϕ and ϕ_0 equal densities of a specimen at time t during sintering and at time t = ∞, respectively. Assume that the shrinkage is isotropic. Then, if the weight of the sample (W) is known, the density ϕ at time t during sintering is related to the linear dimensional change, $\Delta L/L_0$, where $\Delta L = L_0 - L$, L_0 and L are the initial dimension and dimension at time t during sintering, respectively. Then ϕ/ϕ_0 is written

$$\begin{aligned} \phi/\phi_0 &= W/V \;/\; W/V_0 = V_0/V \\ &= 1/(1 - \Delta L/L_0)^3 \end{aligned} \tag{40}$$

or

$$\phi = \phi_0/(1-\Delta L/L_0)^3 \tag{41}$$

2.4.4 Vacancy concentration gradients

2.4.4.1 The average vacancy concentration gradients

All of the factors in equation (36) may be experimentally determined or obtained from the literature except $\langle\vec{\nabla}C_S\rangle$, the average value of the vacancy concentration gradient over the pore-solid interface.

Rearranging equation (36) gives

$$\langle\vec{\nabla}C_S\rangle = \left(\frac{dV_V^P}{dt}\right) / [\Omega^\circ \bar{f} D_V \cdot S_V^{sp}(1 + y)] \tag{42}$$

where $y \equiv \frac{bD_b}{D_V} \cdot \frac{L_V^{ssp}}{S_V^{sp}} \cdot \frac{\langle\vec{\nabla}C_b\rangle}{\langle\vec{\nabla}C_S\rangle}$.

The unit of $<\vec{\nabla}C_S>$ is vac/cm^3/cm. Strategies for obtaining the values of $<\vec{\nabla}C_S>_{kin}$, i.e. the values of all parameters in the right hand side of equation (42), are summarized in Table 3.

The measurements of the values of parameters which are obtained experimentally are described in Chapter 3. The analysis of vacancy diffusivities is described in the next section.

2.4.4.2 Vacancy diffusivities

Extensive references in the literature[29-32] exist about the experimental determination of diffusion coefficients of Ni, including grain boundary diffusion coefficients and self-diffusion coefficient of Ni. However, no literature exists about the empirical determination of vacancy diffusivities of Ni.

The self-diffusivity of an element generally may be written

$$D^M_{vol} = D_0 \exp - \frac{Q_{SD}}{RT} \tag{43}$$

where D_0 is the preexponential term representing a frequency factor in cm/sec^2; Q_{SD}, the activation energy for the diffusion of a metal in its lattice in kcal/mole; R, the gas constant; and T, the absolute temperature.

Experimental values for the preexponential factor are not available for vacancy diffusion in nickel. However, within errors which are involved in an empirical rule[33] D_0 of the self-diffusion of Ni in lattice may be used for D_0 of the self-diffusion of a vacancy in Ni lattice.

Table 3
Sources of information for factors required to estimate $<\vec{\nabla} C_S>$kin

Methods	Parameters	Remarks
1. Experiments	1) dV_V^P/dt	in-situ measurement of shrinkage
	2) $\bar{f}(S_V^{ss}$ and $S_V^{cell})$	standard stereological counting methods
	3) S_V^{sp}, L_V^{ssp}	
2. Literature	1) $\Omega°$, b	Reference 30 and 34
	2) D_V^{vac}	Equation 49
3. Assumptions	1) $\frac{<\vec{\nabla} C_b>}{<\vec{\nabla} C_S>}$	$\frac{<\vec{\nabla} C_b>}{<\vec{\nabla} C_S>} \approx 1$
	2) $[\frac{Db}{D_V}]^{vac}$	$[\frac{Db}{D_V}]^{vac} \approx [\frac{Db}{D_V}]^{solid}$

The activation energy for the self-diffusion of Ni in a Ni lattice may be separated into two parts,

$$Q_{SD} = \Delta H_m + \Delta H_v \tag{44}$$

where ΔH_m and ΔH_v are respectively the enthalpy change for the motion and creation of vacancy for one mole of Ni. The vacancy formation energy contributes to the activation energy for diffusion of a metal atom because its motion requires the presence of a vacant site. The probability that an adjacant site is vacant involves the factor $\exp(-\Delta Hv/RT)$. This factor (or an analogous one) is not required in the formulation for the diffusion of a vacancy since (almost) all sites adjacent to a vacancy are occupied by atoms. Thus the activation energy for vacancy diffusion is

$$Q_{SD}^{vac} \text{ in Ni} = \Delta H_m \text{ in Ni} \tag{45}$$

Experimental observations[35] have demonstrated that for close-packed structures the energy of motion of a vacancy is 0.43 of the activation energy for self-diffusion. Therefore

$$\begin{aligned} Q_{SD}^{vac} \text{ in Ni} &= \Delta H_m \text{ in Ni} \\ &= 0.43\ Q_{SD} \end{aligned} \tag{46}$$

Theories of microstructural evolution during sintering were reviewed with an emphasis on the geometrically general kinetic theory together with the strategies used to relate the model with an experimental demonstration in this chapter. Experimental procedure used to obtain the value of parameters associated with the experimental demonstration is followed in the next chapter.

CHAPTER 3
EXPERIMENTAL PROCEDURE

3.1 Introduction

Sample preparation, microstructural characterization of the sample and the in-situ measurement of densification required for the analysis of the kinetics of microstructural evolution are described in detail in this chapter.

3.2 Sample Preparation

This section presents the procedure employed to prepare presintered samples, sintered samples and the standard for density measurements.

3.2.1 Presintered samples

Two types of samples of pre-sintered nickel powder were prepared by loose stack sintering: one series of sintered samples was prepared for stereological analysis and the other for the in-situ kinetic measurement of shrinkage. The initial volume fraction of solids of all samples was $V_V^s = 0.800 \pm 0.005$ obtained by sintering for 9 minutes at 1250°C. The same powder as used in previous work,[19,20] INCO type 123 nickel powder, (Figure 6) supplied by International Nickel Company, Inc., with the chemical and physical properties listed in Table 4, was used to produce both types of presintered samples.

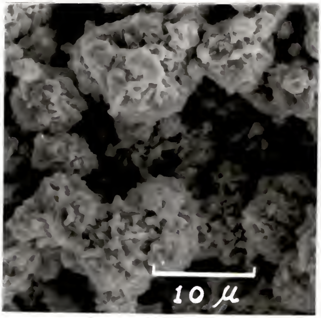

Figure 6. INCO 123 nickel powder used in the present investigation.

Table 4
Characteristics of INCO type 123 nickel powder[36]

Chemical composition	Weight %
Carbon (typical)	0.03-0.08
Carbon	0.1 max
Oxygen	0.15 max
Sulfur	0.001 max
Iron	0.01 max
Other Elements	trace
Nickel	balance

Physical properties

Particle shape - Roughly spherical with spiky surface

Average particle size (Fisher subsieve size)	4-7 micron
Apparent density	1.8-2.5 g/cc
Surface area per unit volume	7.31×10^3 cm^2/cm^3
Typical angle of repose	62°

3.2.1.1 Presintered samples for stereological measurement

In order to produce a series of sintered samples having densities that are uniformly distributed over the range V_V^S = 0.890~0.974, a presintered sample was produced by heating a loose stack powder (tapped to yield a level top surface) in an alumina boat (6 x 12 x 75 mm) under a flowing dry hydrogen atmosphere for 9 minutes. This presintered sample was cut into a number of small pieces (each about 5 mm thick); the density of each piece was determined by the Archimedes method. Those pieces of sample having solid volume fractions outside the range of 0.800±0.005 were discarded.

3.2.1.2 Presintered samples for the in-situ measurement of shrinkage

A presintered sample having a cylindrical shape was fabricated by heating a loose stack powder (tapped to yield a level top surface) in a specially designed fused silica mold (15 mm IH x 12 mm ID x 1.5 mm TH) that is set on the mid-section of the alumina boat, as illustrated in Figure 7 under a flowing dry hydrogen atmosphere for 9 minutes. Those presintered samples with solid volume fractions in the range 0.800±0.005 were selected for subsequent kinetic measurements. Bottom and top surfaces were ground and polished in order to minimize surface roughness and rounded edges.

3.2.2 A series of sintered samples for stereological characterization

The first sample of the series was prepared by heating the set of presintered samples accepted for processing in an alumina boat under a flowing dry hydrogen atmosphere for the preselected sintering time at 1250°C. The boat was then removed from the furnace and the first piece

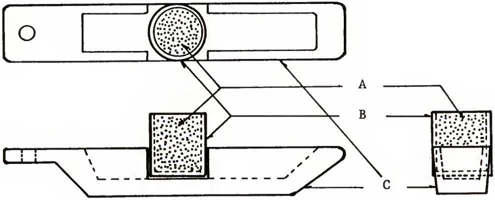

Figure 7. A boat set-up for the fabrication of the presintered specimen used for in-situ shrinkage measurement.
A : Tapped powder
B : A fused silica mold
C : An alumina boat, the mid area of which has been removed

of sample was picked up and set aside for subsequent characterization. The alumina boat with the rest of the pieces of the presintered body was reinserted into the furnace and sintered further. Repetition of this procedure for an appropriate sequence of accumulated sintering times yielded the set of samples used for characterization. It required 11 minutes for the sample transferred from the cold zone to the hot zone to reach the sintering temperature. Although this time was not negligible when compared to the time spent at the sintering temperature and although this procedure takes the samples through an increasing number of heating and cooling cycles with longer sintering times, it has been shown that these cycles do not influence the path of microstructural change in metal powders.[37]

3.3 Characterization of the Sample

Both a standard water immersion method[28] and the standard stereological counting method[38] were employed in order to obtain V_V^P. The standard stereological counting methods and fundamental relationships of quantitative microscopy depicted in Table 5 were used in order to characterize the sample stereologically. Serial sectioning analysis[19,21] was employed to obtain the topological properties. A total of seven samples having densities uniformly distributed over the range from $V_V^S = 0.889$ to 0.974 were characterized.

3.3.1 Density

A standard water immersion procedure[28] was employed in order to measure the density of porous samples. The principle of the procedure is based on the Archimedean principle that the volume of water displaced

Table 5
Fundamental relationships of quantitative stereology[38]

Geometric Property in unit volume	Symbol	Units	Measuring Relationship	Quantities Measured on Section
Volume Fraction	V_V	cm°	$V_V = P_P$	P_P = Fraction of points of a grid that fall in a phase of interest
Area of Surface	S_V	cm^{-1}	$S_V = 2P_L$	P_L = Number of intercepts that a test line of unit length makes with the trace of a surface on a plane section
Length of Line	L_V	cm^{-2}	$L_V = 2P_A$	P_A = Number of points of emergence of linear feature per unit area of plane section
Curvature of Surface	M_V	cm^{-2}	$M_V = \pi T_A$ $= 2\pi N_A$	T_A = Net number of times a sweeping test line is tangential to the convex and concave traces of surface per unit area of a plane section
				N_A = Number of full features that appear on a section of a unit area

when the sample is immersed in water is numerically equal to the decrease in weight of the sample when immersed. The procedure is summarized as follows.

After the sample is weighed in air (W_1), it is coated with wax and weighed again (W_2). The wax-coated sample is placed in the miniature pan in a beaker of distilled water and weighed (W_3). The sample is then dropped to the bottom of the beaker by gently tilting the pan. The weight of the partially immersed pan (W_4) is measured. The density of the sample, ϕ, is calculated as follows:

$$\phi(g/cc) = \frac{W_1}{W_2 + W_4 - W_3} \tag{47}$$

The weight of a thin coating of paraffin wax typically was equal to a few tenths of a percent of the weight of the sample. An electronic balance accurate to ±0.1 mg was used. The density of each sample was measured at least three times. If the differences of the three measurements were within ±0.5%, then the value of density was accepted for further process.

3.3.2 Metric properties

Two groups of metric properties were measured by standard stereological counting methods:[38] one group ($V_V{}^{P}$, $S_V{}^{sp}$, $M_V{}^{sp}$) was determined on the polished surface; the other group ($S_V{}^{ss}$, $S_V{}^{cell}$, $L_V{}^{ssp}$) required an etched surface.

3.3.2.1 Polishing procedure

The wax coating on the sample was dissolved in hexane. The sample was surrounded by a nickel ring and mounted in epoxy. The purpose of the nickel ring will be discussed later in this section. Rough polishing was done on wet silicon carbide papers of increasing fineness from 180 grit through 600 grit. Fine polishing was done by using 6 micron diamond paste, followed by 1 micron diamond paste and finally 0.25 micron diamond paste.

3.3.2.2 Group one measurements ($V_V{}^P$, $S_V{}^{SP}$, and $M_V{}^{SP}$)

Prior to measuring the group one metric properties, the polished surface of each sample was calibrated by measuring the volume fraction of porosity by quantitative stereology and comparing the result with the value obtained from Archimedean density measurements. The sample preparation was accepted for further characterization if the metallographically determined $V_V{}^P$ was within ±2% of $V_V{}^P$ obtained from the water immersion method. Measurements of $S_V{}^{SP}$ and $M_V{}^{SP}$ were made on the accepted polished surfaces using standard techniques.~~[36]~~[38] The measurements of $V_V{}^P$, $S_V{}^{SP}$ and $M_V{}^{SP}$ were made on at least 30 different fields and at a magnification of 500. A square grid with seven divisions on each side (i.e. 36 small squares and 49 points) was used. Point counting for $V_V{}^P$ was done on 4 x 4 squares (i.e. 25 points). Four sides of the 4 x 4 square were used for the line intercept counts. Tangent counts were done on an area of 4 x 4 squares.

3.3.2.3 Group two measurements (S_V^{ss}, S_V^{cell}, L_V^{ssp})

Measurement of the metric properties (V_V^P, S_V^{sp}, and M_V^{sp}) was followed by etching the specimens to reveal the grain boundaries. Each sample was immersed in a solution made from equal parts of nitric acid, glacial acetic acid and acetone for about 15 seconds (at low densities) to about 30 seconds (at high densities). A very short finish polishing with 0.25 micron diamond paste immediately before etching enhanced the quality of the etched surface of the specimen without changing the calibrated value of V_V^P. This finish polish was done manually without applying pressure but with excess lubricant for less than 20 seconds. A major potential source of error in measuring these properties (S_V^{ss}, S_V^{cell}, L_V^{ssp}) was distinguishing between a grain boundary and a twin boundary. Several guidelines[39,40] were used:

1) A grain boundary is usually revealed to be an irregular curve, but a twin boundary is a straight line or less curved on a two dimensional field.
2) Even though a grain boundary ($\tau_G = 870 mJ/m^2$)[41] has 20 times higher energy than a twin boundary ($\tau_T = 40 mJ/m^2$),[41] a twin boundary is revealed to be darker than a grain boundary on the etched surfaces under the microscope fields.
3) At the triple point the angle between adjacent boundaries is close to 120° for a grain boundary but far less or far greater than 120° for a twin boundary.
4) A twin boundary is formed within or across a single grain so that it can be terminated within a grain, but a grain boundary is formed continuously without termination except at a triple point, a pore or out of field.

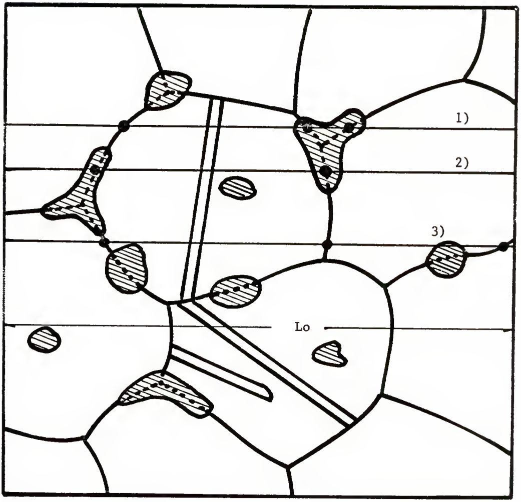

Figure 8. Measurement of cell boundary area and grain boundary area.

1) $P_L^{cell} = 3/Lo$, $P_L^{GB} = 1/Lo$

2) $P_L^{cell} = 2/Lo$, $P_L^{GB} = 0/Lo$

3) $P_L^{cell} = 3/Lo$, $P_L^{GB} = 3/Lo$

5) Development of a quadruple point of a grain boundary usually cannot be detected on a two dimensional field.

A cell boundary area, S_V^{cell}, defined in Chapter 2, illustrated in Figure 8, was measured under the assumptions that all faces of a cell have the grain boundary and by counting line intercept counts (P_L^{cell}) with the assumed cell boundary which includes a grain boundary and an extension of the grain boundary into pores which are occupied along grain boundary networks. The four sides of a 4 x 4 square were used for the line intercept counts; triple point counts were done within the area of the 4 x 4 square. The measurements of group two metric properties were made on at least 30 different fields.

The measurements of pore structure and grain structure metric properties were followed by topological characterization.

3.3.3 Topological properties

The topological properties, connectivity and the number of isolated pores were measured through serial sectioning analysis. During the process of serial sectioning, the group one metric properties (V_V^s, S_V^{sp} and M_V^{sp}) on an intermediate section (the 16th) were measured. This permits assessment of the contributions from isolated pores and those from connected pores to each of these properties. The procedure for serial sectioning is described in this section, followed by the algorithm used for topological analysis.

3.3.3.1 Serial sectioning

The procedure of serial sectioning employed in this investigation was essentially the same as that developed by DeHoff and his students[15]

(Aigeltinger[21] and Watwe[19]). The average thickness of a section used was of the order of one-fifth of that of scale of the structure. Since the reliable measure of the scale of the system is the mean intercept of pore phase,

$$\bar{\lambda}_p = \frac{4V_V^p}{S_V^{sp}}, \tag{48}$$

$\bar{\lambda}_p$ can be obtained from the slope of the straight line in Figure 22. The $\bar{\lambda}_p$ obtained was ≈4.2 microns.

The thickness of a section was monitored by using a microhardness tester. A square-based, pyramid-shaped indentation can be made on the polished surface of a sample. By measuring a change in the length of the diagonal of an impression after polishing, Δd, illustrated in Figure 9, the thickness of a section polished, Δh, can be evaluated from a known relation, $\Delta h = 0.1428\Delta d$. Watwe[19] showed that the extent of polishing (removal of material) of the nickel ring, mentioned in Section 3.3.2.1, and the sample, was not statistically different. The average value of thickness removed from the five equally spaced indentations in the ring was therefore used as the section thickness. Two holes[20] drilled on the sample with a #80 drill bit or the geometrical shape of a specimen contour were used for the purpose of locating the same microscopic field after each polishing step. The geometrical shape of a specimen contour and grid points on the specimen contour were recorded on a separate paper and used in order to locate the same microscopic field. A Buehler ECOMET III polisher with WHIRLMET automatic polishing attachment was used to achieve a combination of speed, load and time that would yield the desired magnitude of material removal. The surface of the sample was conditioned by polishing it on a microcloth with one micron diamond paste

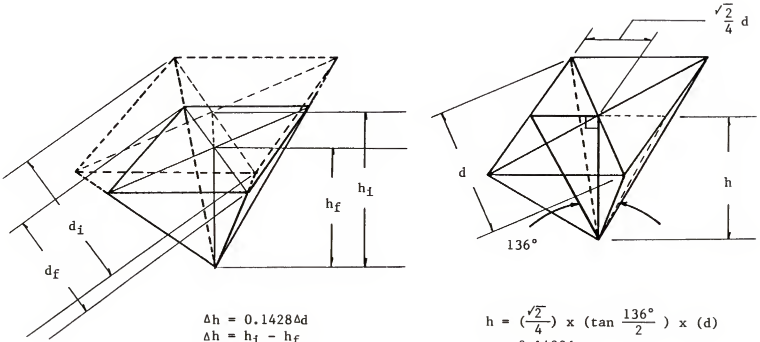

$\Delta h = 0.1428 \Delta d$
$\Delta h = h_i - h_f$
$\Delta d = d_i - d_f$

$h = (\frac{\sqrt{2}}{4}) \times (\tan \frac{136°}{2}) \times (d)$
$= 0.1428d$

Figure 9. The relationship between decrease in the depth of the microhardness indentation and decrease in the length of diagonals of the indentation.

so that all plastic deformation due to the drilling or the etched layer on the surface of the sample might be removed. After cleaning and drying, the sample was ready for photomicrography. A Zeiss ICM 405 metallograph was used for all photomicrographs. A set of 31 4" x 5" Polaroid prints was obtained by repeating the polishing and photographic steps. During the process of serial sectioning, a set of the etched and non-etched surfaces of the sixth section of all the samples was prepared and used for characterization of metric properties ($S_V{}^{sp}$, $M_V{}^{sp}$, $S_V{}^{ss}$, $S_V{}^{cell}$ and $L_V{}^{ssp}$). A complete set of photomicrographs and negatives for the etched and non-etched surfaces of the sixteenth section of all the samples was also obtained and enlarged to a 400 magnification. These photomicrographs were used for the separate characterization of the isolated and connected pores. Since the thickness which was supposed to be removed was limited, the metallographic preparation of the sixth and sixteenth section could not be calibrated.

3.3.3.2 Topological analysis

The basic idea employed for a topological analysis, originated by DeHoff[15] and Aigeltinger[21] and modified by Watwe,[19] was based on two concepts. First, the maximum and minimum limits on the estimate of connectivity (Genus) were imposed since it is not possible to determine whether pore sections intersect each other or meet with themselves outside the volume covered by the series of parallel areas of observation. As illustrated in Figure 10, an upper limit on connectivity, G^{max}, is obtained when all the pores meeting the boundaries of the volume of analysis are regarded as meeting at a common external node. On the other hand, a lower limit, G^{min}, is derived by considering

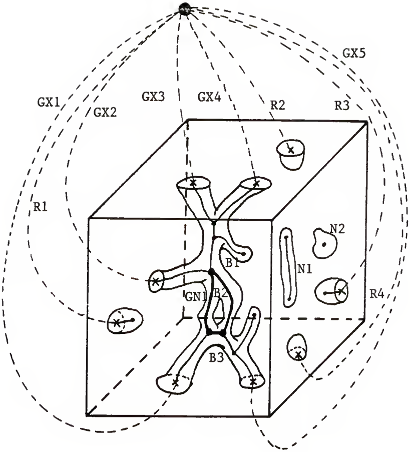

Figure 10. Basic idea for the estimation of G^{max}, G^{min}(GN) and N^{iso}. G^{max} = 6(=5GX + 1GN). R refers to the redundant connections to be deleted from the estimate of G^{max}. B refers to branching and N, isolated pores. G^{min}=1(=1GN), N^{iso}=2(=2N).

all such pores to be terminating or "capped" at the boundaries. The quantity of G^{min} therefore consists solely of redundant connections or "loops" observed within the volume of analysis. Secondly, the number of separate parts, as illustrated in Figure 10, is obtained by counting the separate pores that are contained solely within the volume observed and do not intersect the boundaries.

A set of 4" x 5" Polaroid prints was enlarged a number of times by Xerographic reproduction. An area which contained about 100 pores was marked on the center of the first print and the same rectangular area was marked on the successive prints such that the pores observed on the consecutive sections were in the same position relative to the boundaries of the rectangle.

The actual analysis is illustrated in Figures 11 and 12. The pores observed in section 1 are numbered beginning with 1R (Figure 12-a). Each of these pores contributes +1 to ΔG^{max}, as shown in Table 6. The pores that first appeared thereafter on successive sections are numbered beginning with 1B (Figure 12-c). These appearances of new pores inside the boundary plane contribute to none of the topological properties (case no. 2 in Table 6, sections 2, 3 and 4 in Figure 11). But when these pores which appeared inside the boundary disappear by comparing pairs of neighboring sections, each of them contributes +1 to ΔN^{iso}, the number of isolated pores (case no. 4 in Table 6, sections 5 and 7 in Figure 11). On the contrary, the disappearance of a pore which appeared on the boundary plane contributes -1 to ΔG^{max}, since as illustrated in Figure 10, this disappearance does not form any possible loop that is assumed to exist outside the volume of analysis (case no. 3 in Table 6, sections 2 and 7 in Figure 11).

Table 6
Events that may occur during a serial sectioning analysis and contributions to the topological properties[21]

Category	Change in the ith section	contributions to			case No
		ΔG^{max}	ΔG^{min}	ΔN^{iso}	
whole network	. appearance of a new pore on the boundary plane or line	+1	0	0	1
	. appearance of new pore inside the boundary area	0	0	0	2
	. disappearance of a pore which appeared on the boundary	-1	0	0	3
	. disappearance of a pore which appeared inside the boundary	0	0	+1	4
within a subnetwork	. splitting a pore forming a branch	+1	0	0	5
	. termination of an offspring of a branch	-1	0	0	6
between a subnetworks	. connection between different or new subnetworks	0	0	0	7
	. connection between same subnetworks	0	+1	0	8

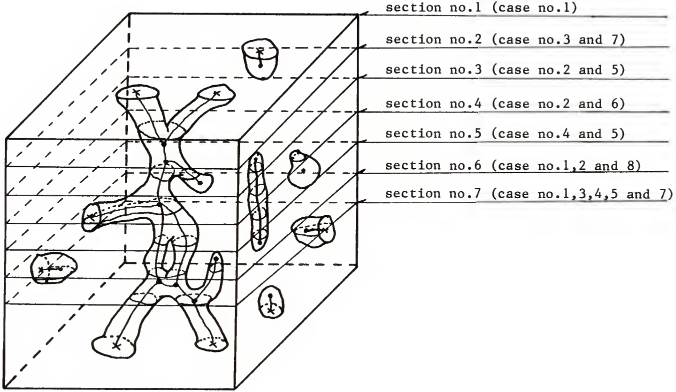
section no.1 (case no.1)
section no.2 (case no.3 and 7)
section no.3 (case no.2 and 5)
section no.4 (case no.2 and 6)
section no.5 (case no.4 and 5)
section no.6 (case no.1,2 and 8)
section no.7 (case no.1,3,4,5 and 7)

Figure 11. Schematic of a serial sectioning analysis of the sample in Figure 10, where case no. is in Table 7.

Within a subnetwork, a branch may occur. Appearance of a branch contributes +1 to ΔG^{max} (case no. 5 in Table 6, sections 3, 5 and 7 in Figure 11), since the number of possible loops, terminating in a single external node, is increased by one, as shown in Figure 10. When such a branch is observed to disappear ΔG^{max} is decreased by one in order to account for the increase assumed prior to an observation of this event (case no. 6 in Table 6, section 4 in Figure 11).

A connection between unconnected subnetworks, those with different numbers (section 2 and section 7 in Figure 12), does not contribute to any of the three properties (case no. 7 in Table 6). A connection between two or more subnetworks with the same number forms a complete loop observed entirely inside the sample volume (section no. 6 in Figures 11 and 12) and contributes +1 to ΔG^{min} (case no. 8 in Table 6). But it does not contribute to ΔG^{max} because ΔG^{max} was already increased by one when the original branching occurred.

The accumulated values of G^{max}, G^{min} and N^{iso}, as illustrated in Figure 12, were used in order to get the unit volume quantities G_V^{max}, G_V^{min} and N_V^{iso}. In order to get these unit volume quantities the size of sampling volume where the serial sectioning analysis should be terminated needs to be known. Two types of criteria[15,19] have been proposed and used. The first one[21] proposed and used was a linearity in the plot of the accumulated quantities versus the accumulated volume analyzed. The second criterion[19] was the constancy of the volume tangent counts. From both[19,21] of the previous works and other works,[20,22] 30 sections were found to be sufficient to fulfill the two types of criteria.

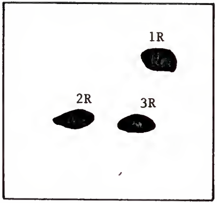

a) section no.1

* ΔG^{max}	ΔG^{min}	ΔN^{iso}
-	-	-
3	0	0
3	0	0

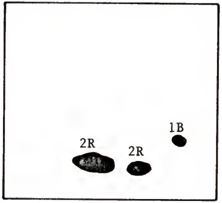

c) section no.3

ΔG^{max}	ΔG^{min}	ΔN^{iso}
2	0	0
+1	0	0
3	0	0

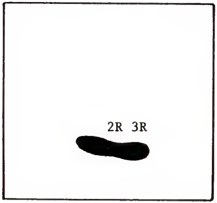

b) section no.2

ΔG^{max}	ΔG^{min}	ΔN^{iso}
3	0	0
-1	0	0
2	0	0

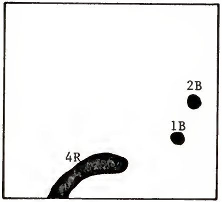

d) section no.4

ΔG^{max}	ΔG^{min}	ΔN^{iso}
3	0	0
-1	0	0
2	0	0

Figure 12. Schematic of a toplogical analysis of the sample in Figure 11.

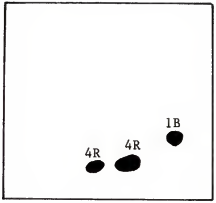

e) section no.5

ΔG^{max}	ΔG^{min}	ΔN^{iso}
2	0	0
+1	0	+1
3	0	1

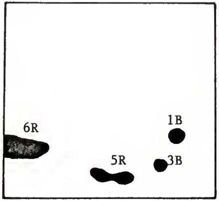

f) section no.6

ΔG^{max}	ΔG^{min}	ΔN^{iso}
3	0	1
+2	+1	0
5	1	1

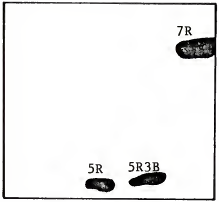

g) section no.7

ΔG^{max}	ΔG^{min}	ΔN^{iso}
5	1	1
+1 -1 +1	0	+1
6	1	2

*	ΔG^{max}	ΔG^{min}	ΔN^{iso}	ΔVi
previous total	-	-	-	-
current section	-	-	-	-
current total	-	-	-	-

R : red color
B : blue color
ΔV_i: volume of section

Figure 12. Continued from the previous page.

The unit volume quantities were also obtained from the slopes in plots of the accumulated topological quantities versus accumulated volume analyzed. The analyzed volume for each sample was about [10^{-6} cm^3].

3.3.4 Metric properties on intermediate serial sections

The metric properties (both group one and group two) were measured on two intermediate sections obtained during serial sectioning analysis. In order to obtain a good polished and etched surface within the limit of polishable thickness, the manual finish polishing was carefully controlled so that artifacts might be minimized within the limit of the degree of polishing.

It is possible to distinguish connected porosity from the isolated pores on any of the series of sections used for topological analysis. As illustrated in Figure 13, the "connected" porosity includes all pores that were not wholly contained in the volume of analysis. Therefore, the actual measurement of the connected properties was performed after all the series of sections were obtained and analyzed. Typically the number 16th section of each sample was chosen in order to measure the connected properties. The measured connected properties include the group one metric properties (V_V^P, S_V^{SP}, and M_V^{SP}). Since the number 16th section could not be calibrated within the limited thickness of polishing, the ratios V_V^{conn}/V_V^{tot}, S_V^{conn}/S_V^{tot} and M_V^{conn}/M_V^{tot} were estimated and multiplied by the V_V^P, S_V^{SP}, and M_V^{SP} values obtained on the calibrated surfaces.

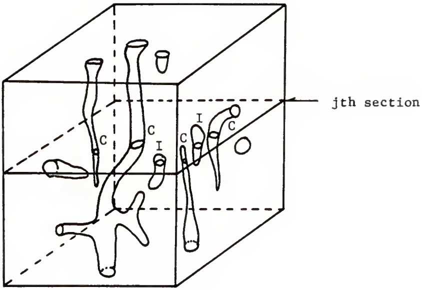

(a) Sampling volume

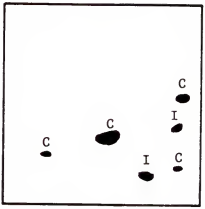

(b) jth section

Figure 13. Distinguishing between a connected pore (C) and an isolated pore (I).

3.4 In-situ Measurements of Shrinkage

3.4.1 Introduction

Even though the procedure employed in order to produce a series of sintered sample involved heating and cooling cycles, these cycles have been shown to have no influence on the path of microstructural change.[37] In contrast, the kinetics associated with the above mentioned samples may be sensitive to the heating and cooling cycles. In order to rule out the uncertainties associated with heating and cooling cycles during the fabrication process of the series of sintered samples, an in-situ measurement of shrinkage was undertaken. A photographic method was employed in order to monitor in-situ dimensional change of the presintered cylindrical sample during sintering.

3.4.2 Monitoring the in-situ dimensional change

Measurement of the dimensional change during sintering, illustrated in Figure 14, was carried out on a series of photographs of the sample during sintering. An observation window attached to the end of the fused silica furnace tube was designed to give access to the in-situ image of the sample in the hot zone (1250°C±5°C) of the furnace. A camera (MINOLTA XM 570) with a 210 mm zoom lens was used. In order to minimize the blurring effect of the boundary of the image due to radiation from the hot specimen and the fused silica tube surrounding the specimen, a polarizer filter was used. An automatic remote shutter release was employed. An optimum condition for photographing, using B/W film, ASA 400, f/32 and 1/15 sec for exposure, was obtained by trial and error. The boat and support for the specimen were modified in order to present an optimum position for the specimen during sintering. A series of

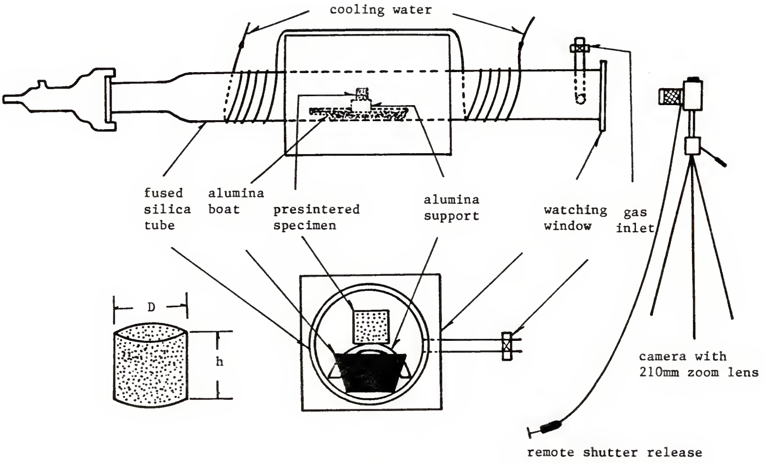

Figure 14. The set-up for monitoring in-situ dimensional change during sintering. ASA 400 black and white film,f/32 and 1/15 sec was used.

photographs were taken during sintering according to the predetermined time schedule; a total of 34 photographs were taken over a period of 824.4 minutes at 1250°C. The first shot was taken when the sample reached the sintering zone by putting the specimen on the prefocused position which was marked on the pushing rod before the start of heating and using the remote shutter release. No additional focusing was done since this may change the apparent dimensions of the image of the sample not from densification. The time lag in taking the first picture was 3 sec, which is negligible with respect to 1 minute, the shortest interval between neighboring shots. Therefore, the dimension in the first shot was negligibly different from the dimension of the presintered specimen having initial density ($V_V^s = 0.795$) at 1000°C (preheating zone), not at 1250°C. As a result, a thermal expansion effect was compensated for the image in the first shot.

Acquisition of a series of dimensions of the in-situ specimen during sintering was done from the images on the photographs which are magnified 2.593 times. An electronic digital vernier caliper, having an accuracy to 0.005 mm, was used in order to measure dimensions.

The density of the sample was measured before and after sintering by the water immersion method. The dimensions of the sample were also measured before and after sintering. Comparisons of the changes in the diameter and the height of the sample after sintering showed that the shrinkage was isotropic.

CHAPTER 4
EXPERIMENTAL RESULTS

4.1 Introduction

The experimental results obtained in the present study are presented in this chapter. The paths of the microstructural evolution during sintering were essentially a reproduction of Watwe's work,[19] except for the determination of the cell boundary area, S_V^{cell}, which was measured for the first time in this investigation. The efficiency factor, which is related to S_V^{cell} and S_V^{ss}, therefrom may be evaluated. The topological properties showed similar trends, but not exact reproductions, of the former work.[19] The path information obtained during the serial sectioning analysis showed some deviations from the same information on the calibrated surfaces, as expected. The analysis of the behavior of pores during the serial section analysis confirmed the finding[19] that it is the isolated pores that disappear in the late stages of sintering of this nickel powder; the network pores remain. Variations of volume fraction of pore, pore-solid interface area and integral mean curvature with sintering time provided a linear relation between the values of these properties and logarithms of sintering time.

The kinetics determined by the in-situ measurement of shrinkage gave little difference from those measured on the series of discontinuously sintered samples. A linear relation in the plot of volume fraction of porosity versus the logarithm of sintering time was ascertained in the range of study for both sintering scenarios. However, the slope of the straight line fitted by the least square method showed a somewhat lower value in a continuous sintering than the value obtained in a discontinuous sintering, i.e. a series of sintered samples. The densification rate may be obtained from in-situ kinetics in terms of variations of volume of pore phase per mole of nickel per second.

The combinations of paths, topological properties and kinetics may be used in order to assess the validity of the cell model; this test is described in the next chapter.

4.2 Microstructures

Figures 15 through 21 illustrate the structure of pores and grain boundary networks of the series of sintered samples. The change of density, i.e. the volume fraction of solid phase, and the shape of pores and grains were observed as the sintering time increases: 1) density increases; 2) pore structures become coarser; and 3) grain size increases.

4.3 Paths of Microstructural Evolution

The measured values of path information are summarized in Table 7. The variations of the pore-solid interface area per unit volume and the integral mean curvature of pore-solid interface per unit volume with volume fraction of solid phase are illustrated in Figure 22 and Figure 23, respectively. Comparisons between the results by Watwe[19] and those of the present study showed no significant differences. All data points are the same within 95% confidence intervals.

The dependence of a grain boundary area (S_V^{SS}) and a cell boundary area (S_V^{cell}) per unit volume on the volume fraction of solid are

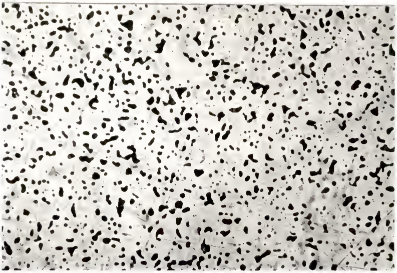

(a)

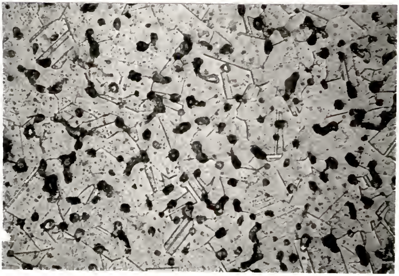

(b)

Figure 15. Photomicrographs of INCO 123 nickel powder loose stack sintered at 1250°C to V_V^S=0.890, (a) unetched (x200) and (b) etched (x500).

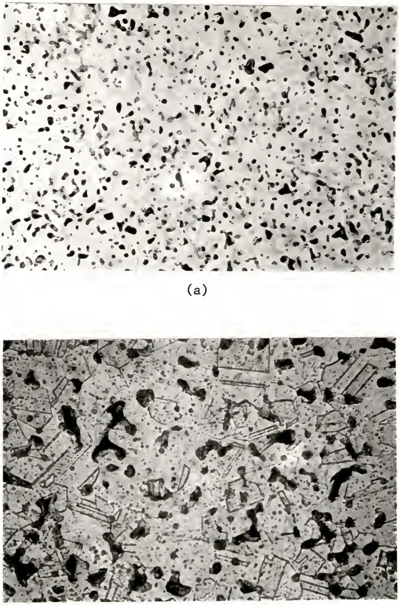

(a)

(b)

Figure 16. Photomicrographs of INCO 123 nickel powder loose stack sintered at 1250°C to V_V^S=0.914, (a) unetched (x200) and (b) etched (x500).

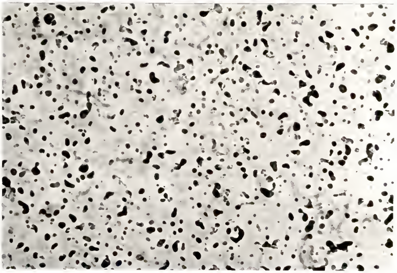

(a)

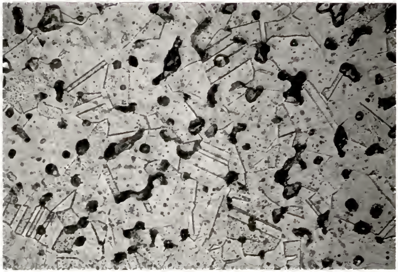

(b)

Figure 17. Photomicrographs of INCO 123 nickel powder loose stack sintered at 1250°C to V_V^S=0.935, (a) unetched (x200) and (b) etched (x500).

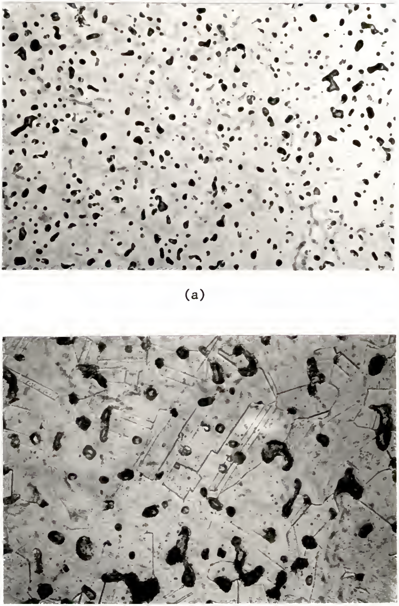

(a)

(b)

Figure 18. Photomicrographs of INCO 123 nickel powder loose stack sintered at 1250°C to V_V^S=0.946, (a) unetched (x200) and (b) etched (x500).

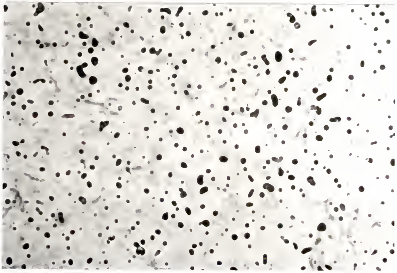

(a)

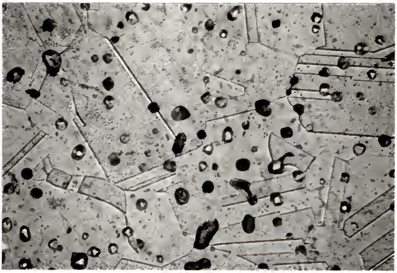

(b)

Figure 19. Photomicrographs of INCO 123 nickel powder loose stack sintered at 1250°C to V_V^S=0.957, (a) unetched (x200) and (b) etched (x500).

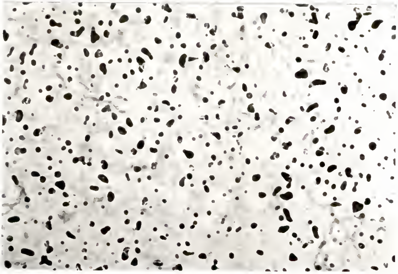

(a)

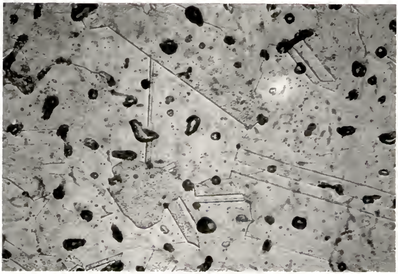

(b)

Figure 20. Photomicrographs of INCO 123 nickel powder loose stack sintered at 1250°C to V_V^S=0.968, (a) unetched (x200) and (b) etched (x500).

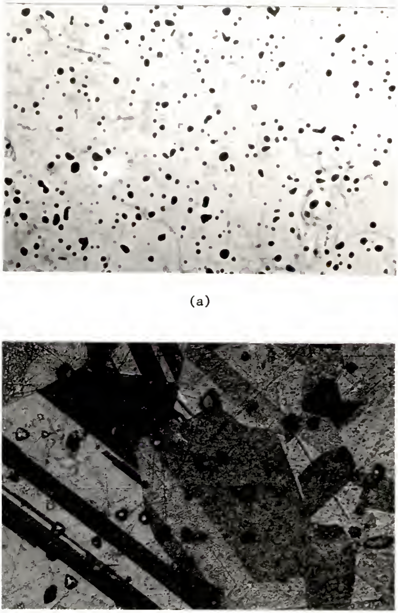

(a)

(b)

Figure 21. Photomicrographs of INCO 123 nickel powder loose stack sintered at 1250°C to V_V^S=0.974, (a) unetched (x200) and (b) etched (x500).

Table 7
Metric properties for INCO 123 nickel powder loose stack sintered at 1250°C in H_2

t(min)	56.4	97.4	159.4	231.4	271.4	316.4	410.4
$V_V^S(cm^o)$	0.890	0.914	0.935	0.946	0.957	0.968	0.974
$S_V{}^{sp}(cm^{-1})$	912.784 ±63.170	735.962 ±77.084	630.824 ±73.302	516.129 ±65.104	415.771 ±57.813	335.125 ±49.422	283.154 ±44.603
$M_V{}^{sp}(10^6cm^{-2})$	2.413 ±0.154	2.144 ±0.124	1.894 ±0.120	1.791 ±0.090	1.359 ±0.088	1.201 ±0.080	1.159 ±0.077
$S_V{}^{ss}(cm^{-1})$	645.161 ±32.307	473.118 ±35.391	408.602 ±27.072	376.344 ±31.552	322.581 ±27.673	313.620 ±23.199	250.896 ±19.784
$S_V{}^{cell}(cm^{-1})$	805.257 ±36.702	585.424 ±46.224	458.781 ±32.025	415.771 ±38.456	354.839 ±26.058	342.294 ±24.484	267.025 ±22.301
$L_V{}^{ssp}(10^5cm^{-2})$	8.907 ±0.668	6.180 ±0.476	3.851 ±0.383	3.353 ±0.281	2.790 ±0.310	2.682 ±0.281	1.611 ±0.318

*mean ± 95% C.I.

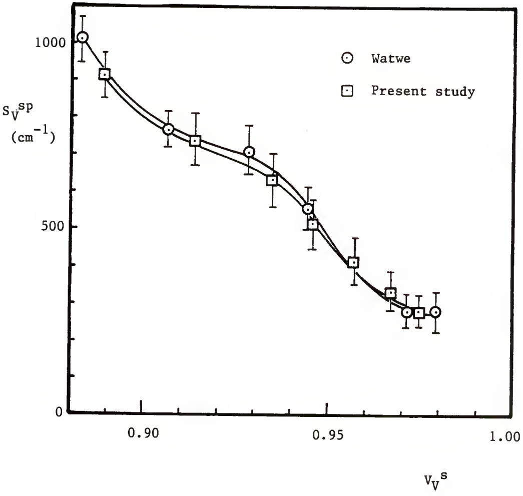

Figure 22. Path of microstructural change for the pore solid interface.

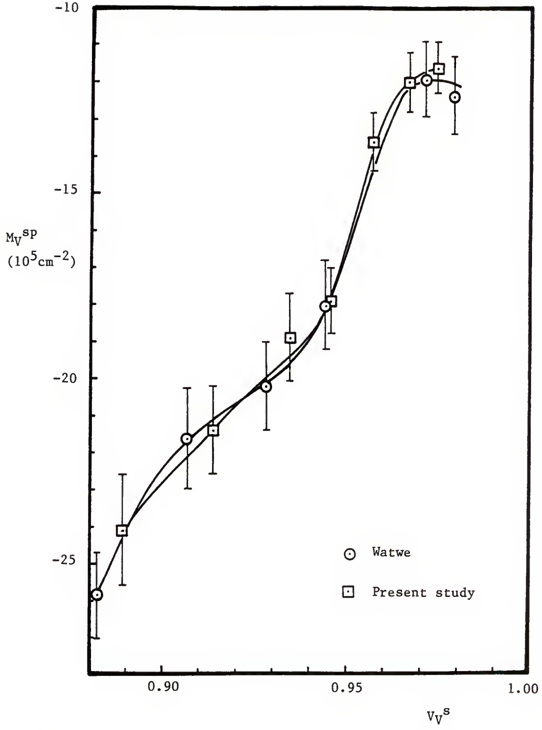

Figure 23. Path of microstructural change for the integral mean curvature per unit volume of the pore-solid interface.

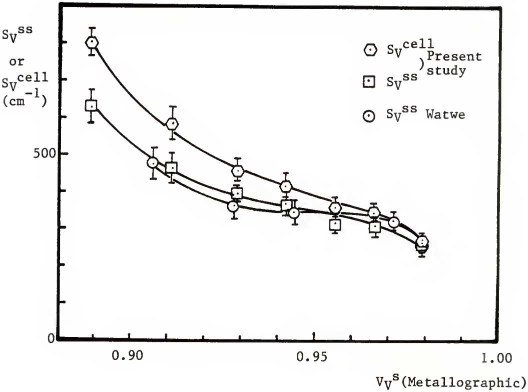

Figure 24. Variations of the surface area and the cell area per unit volume of the grain boundary network with volume fraction of the solid phase.

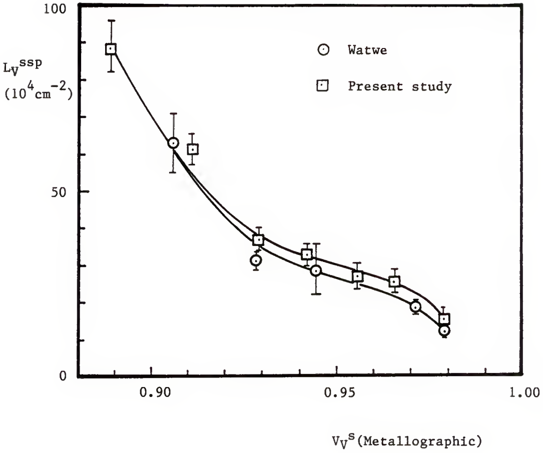

Figure 25. Path of microstructural change of the length per unit volume of triple lines formed by the intersection of grain boundaries with the pore-solid interface.

presented in Figure 24. General trends of the path information of the grain boundary network showed no differences between Watwe's[19] and this study. The gap between the cell boundary area and grain boundary area decreases with densification and essentially disappears at high density. The ratio of cell boundary area per unit volume to grain boundary area per unit volume may represent the efficiency factor, which is evaluated in the next chapter.

A comparison of the paths of microstructural change of the length per unit volume of triple lines formed by the intersection of grain boundaries with the pore-solid interface is presented in Figure 25 for Watwe's and this study.

4.4 Topological Properties

Measured topological properties are summarized in Table 8. Connectivity and the number of isolated pores per unit volume of sample were obtained from both the total volume analyzed and the slope of the least square fitted line in the plot of accumulated topological properties versus accumulated volume analyzed, as illustrated in Figures 29 through 42.

Mean values of both measurements are presented in Figures 26, 27 and 28 for the maximum connectivity per unit volume (G_V^{max}), minimum connectivity per unit volume (G_V^{min}), and the number of isolated pores per unit volume (N_V^{iso}), respectively. Watwe[19] adopted the constancy of volume tangent count criterion for the termination of the serial sectioning analysis, whereas Aigeltinger[21] had adopted the linearity between accumulated topological properties and accumulated volume analyzed as a criterion for the termination. The two measurements by

Table 8
Topological properties of INCO 123 nickel powder loose stack sintered at 1250°C in H_2

V_V^s	*	G_V^{max} ($10^8 cm^{-3}$)	G_V^{max} ($10^7 cm^{-3}$)	$\bar{G}_V$ ** ($10^8 cm^{-3}$)	N_V^{iso} ($10^8 cm^{-3}$)	$\bar{N}_V - \bar{G_V}$ ($10^8 cm^{-3}$)
0.890	1	1.929	5.013		2.516	
	2	1.587	5.474		3.219	
	3	1.758	5.243	1.141	2.867	1.726
0.914	1	1.428	2.597		2.958	
	2	0.657	2.882		3.214	
	3	1.043	2.739	0.658	3.086	2.428
0.935	1	0.882	1.259		4.575	
	2	0.430	1.523		5.136	
	3	0.656	1.391	0.397	4.856	4.458
0.946	1	0.268	1.053		3.914	
	2	0.241	1.331		5.041	
	3	0.254	1.192	0.187	4.478	4.291
0.957	1	0.250	0.625		3.729	
	2	0.104	0.580		4.409	
	3	0.177	0.603	0.119	4.069	3.950
0.968	1	0.412	0.528		2.421	
	2	0.181	0.761		2.682	
	3	0.297	0.644	0.181	2.552	2.371
0.974	1	0.317	0.212		2.148	
	2	-	0.100		2.531	
	3	0.317	0.156	0.167	2.339	2.173

* 1 : from total volume analyzed, 2 : from slope, 3 : mean of 1 and 2

** $(G_V^{max} + G_V^{min})/2$

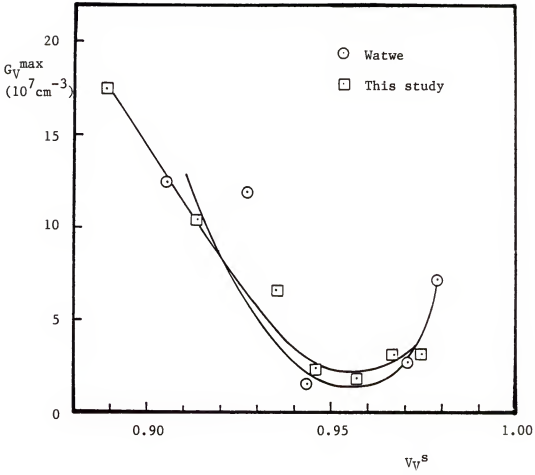

Figure 26. Dependence of maximum connectivity on the volume fraction of solid during loose stack sintering of INCO 123 nickel powder at 1250°C.

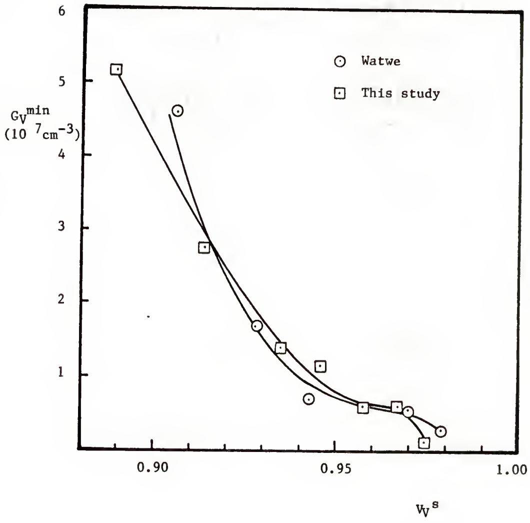

Figure 27. Dependence of minimum connectivity on the volume fraction of solid during loose stack sintering of INCO 123 nickel powder at 1250°C.

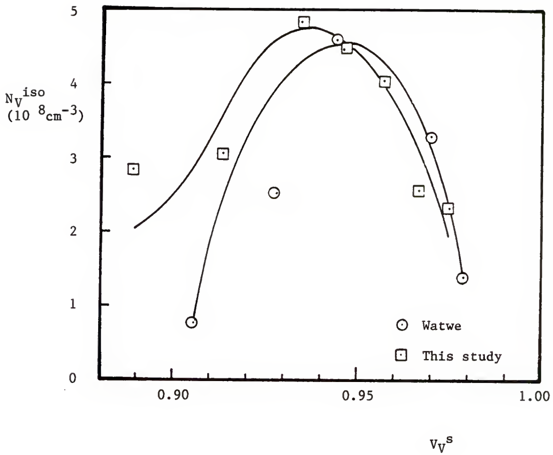

Figure 28. Variation of the number of isolated pores per unit volume with the volume fraction of solid during loose stack sintering of nickel at 1250°C.

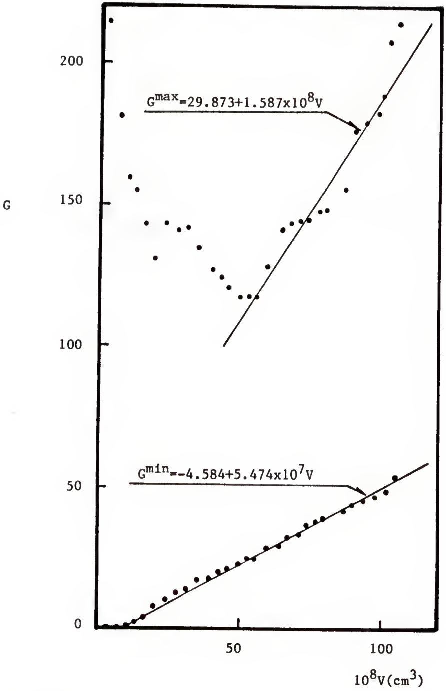

Figure 29. Variation of connectivities with volume analyzed for 5.5 micron nickel powder loose stack sintered to $V_V{}^s=0.890$.

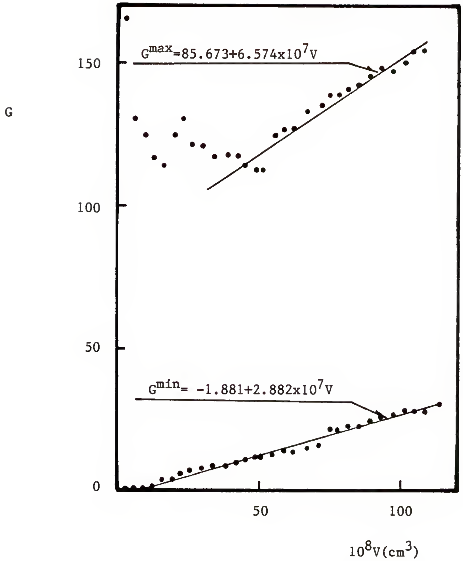

Figure 30. Variation of connectivities with volume analyzed for 5.5 micron nickel powder loose stack sintered to $V_V{}^S=0.914$.

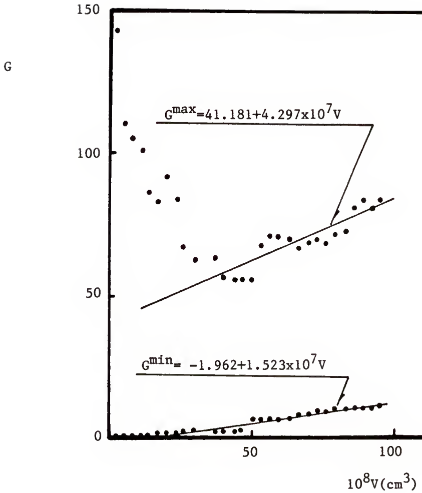

Figure 31. Variation of connectivities with volume analyzed for 5.5 micron nickel powder loose stack sintered to V_V^s=0.935.

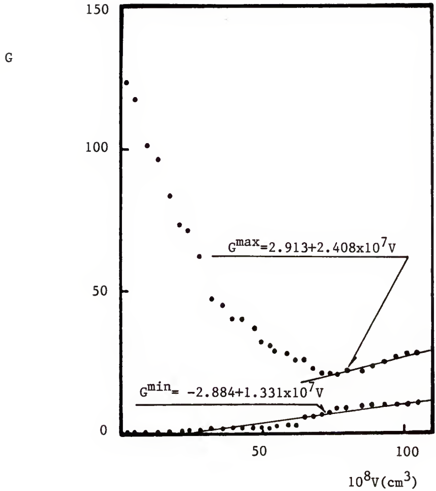

Figure 32. Variation of connectivities with volume analyzed for 5.5 micron nickel powder loose stack sintered to $V_V^S=0.946$.

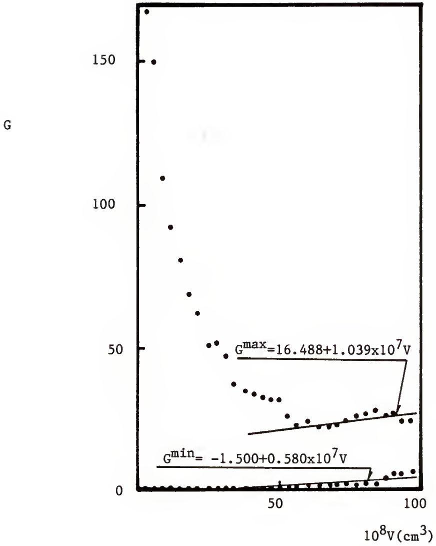

Figure 33. Variation of connectivities with volume analyzed for 5.5 micron nickel powder loose stack sintered to $V_V{}^s=0.957$.

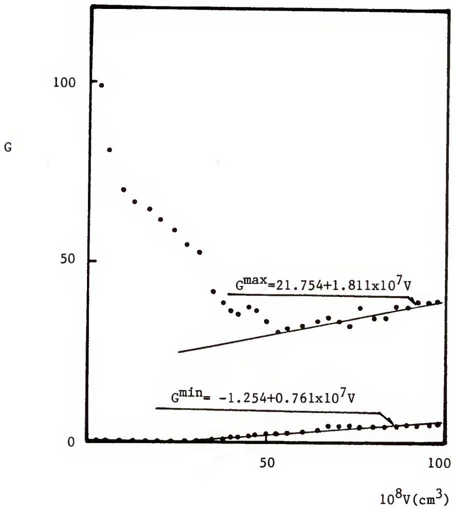

Figure 34. Variation of connectivities with volume analyzed for 5.5 micron nickel powder loose stack sintered to $V_V^s=0.968$.

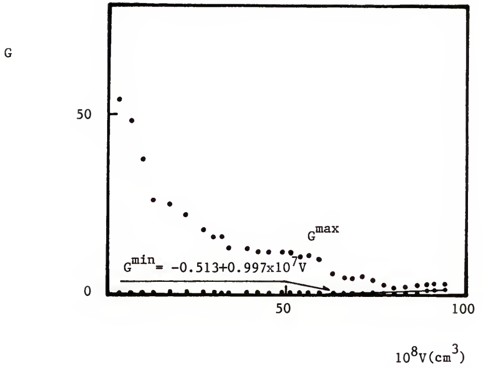

Figure 35. Variation of connectivities with volume analyzed for 5.5 micron nickel powder loose stack sintered to $V_V^S=0.974$.

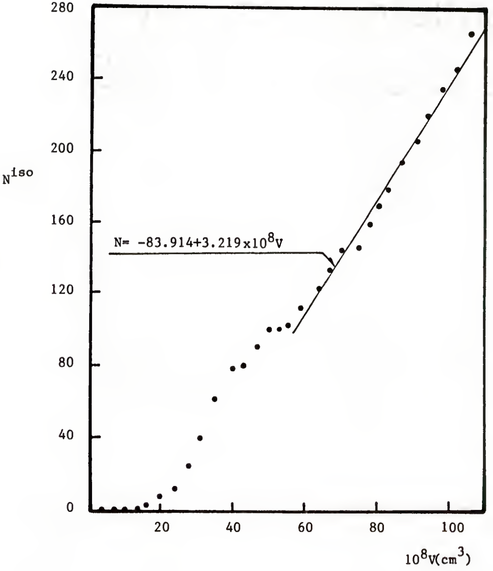

Figure 36. Variation of number of separate parts with volume analyzed for 5.5 micron nickel powder loose stack sintered to $V_V{}^s$=0.890.

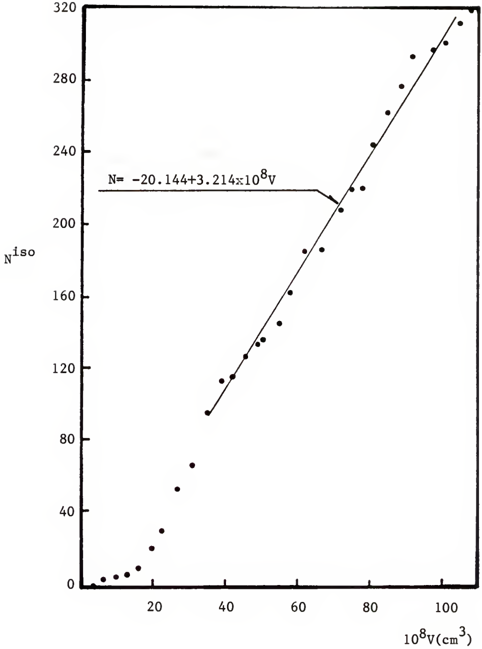

Figure 37. Variation of number of separate parts with volume analyzed for 5.5 micron nickel powder loose stack sintered to $V_V{}^S=0.914$.

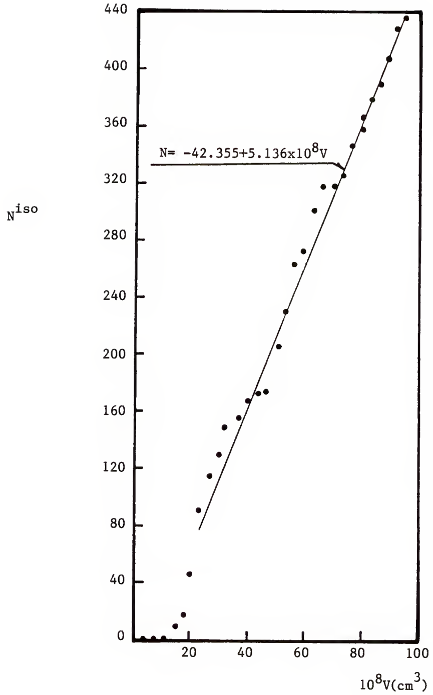

Figure 38. Variation of number of separate parts with volume analyzed for 5.5 micron nickel powder loose stack sintered to $V_V{}^S=0.935$.

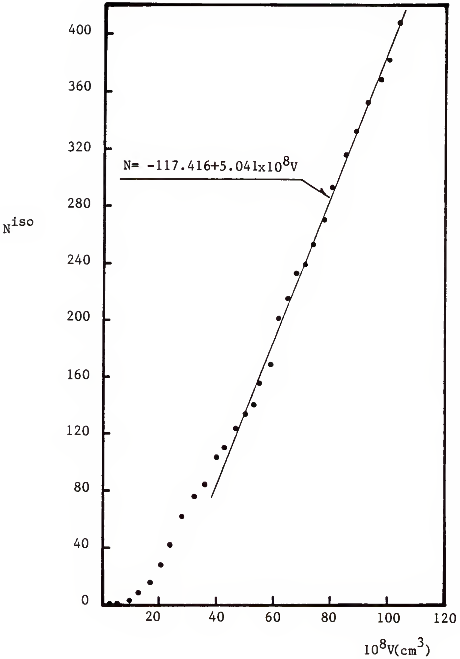

Figure 39. Variation of number of separate parts with volume analyzed for 5.5 micron nickel powder loose stack sintered to $V_V{}^S$=0.946.

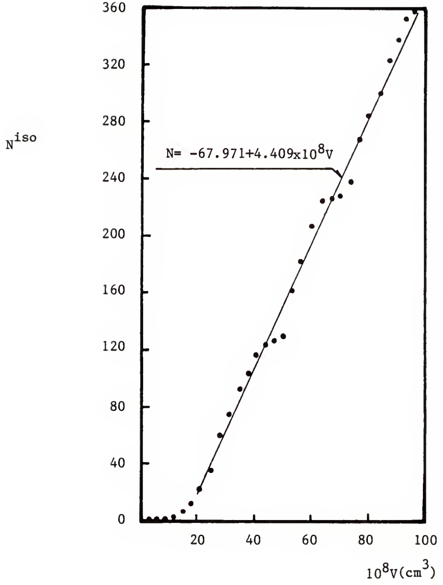

Figure 40. Variation of number of separate parts with volume analyzed for 5.5 micron nickel powder loose stack sintered to $V_V{}^S$=0.957.

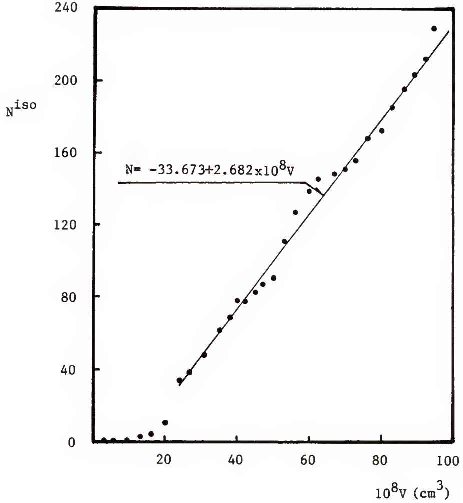

Figure 41. Variation of number of separate parts with volume analyzed for 5.5 micron nickel powder loose stack sintered to $V_V{}^S$=0.968.

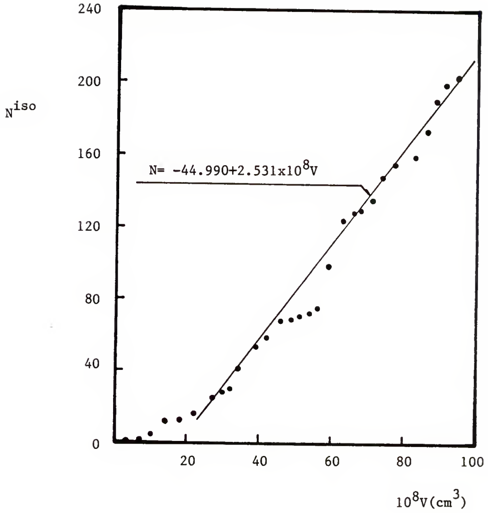

Figure 42. Variation of number of separate parts with volume analyzed for 5.5 micron nickel powder loose stack sintered to V_V^S=0.974.

both criteria should agree. The main sources of errors in characterization of topological properties are related to judgement of the events, inferred to occur between sections. Experimental errors associated with sectioning technique also cannot be excluded completely, for example, measurement of section thickness and photo processing of Polaroid prints are potential sources of error.

Except at a few data points, the general patterns of the variation of topological properties per unit volume with the volume fraction of solid were in agreement with those found by Watwe.

4.5 Path Information obtained from Intermediate Serial Sections

Variations of the metallographically determined volume fraction of connected porosity and isolated porosity with the total volume fraction of porosity are presented in Figure 43. The sum of the volume fraction of connected porosity and that of isolated porosity is constrained to lie along the dashed line. From this observation it is evident that it is the isolated pores that disappear; the network pores remain.[19] In other words, as densification proceeds and pore channels disconnect, pores become isolated, and the part of the volume occupied by isolated pores increases. After some maximum value of the volume fraction of isolated pores their volume fraction decreases and disappears, while the volume fraction of connected pores remain constant.

These observations[19] are rationalized as follows. Network pores are composed primarily of cylindrical segments. When a moving grain boundary encounters a cylinder in any orientation other than that in which the axis of the pore lies in the plane of the boundary, the boundary will not be significantly impeded. This is because translation of the boundary

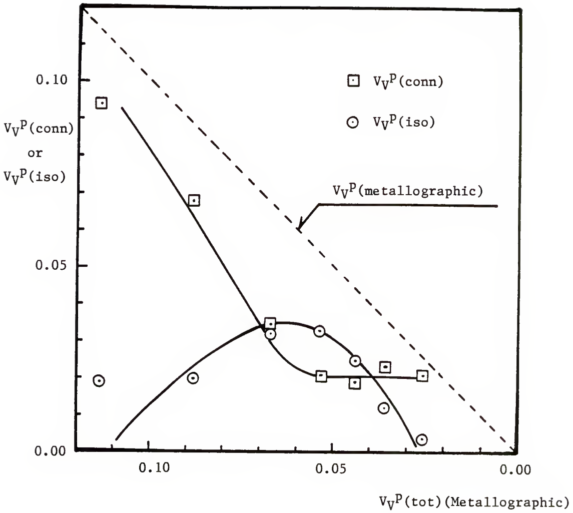

Figure 43. Dependence of the metallographically determined volume fraction of connected porosity and isolated porosity on the volume fraction of porosity.

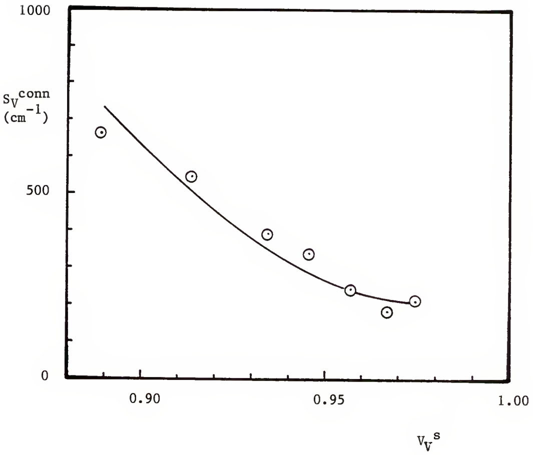

Figure 44. Dependence of surface area of the connected porosity per unit volume on the volume fraction of solid during loose stack sintering of nickel at 1250°C.

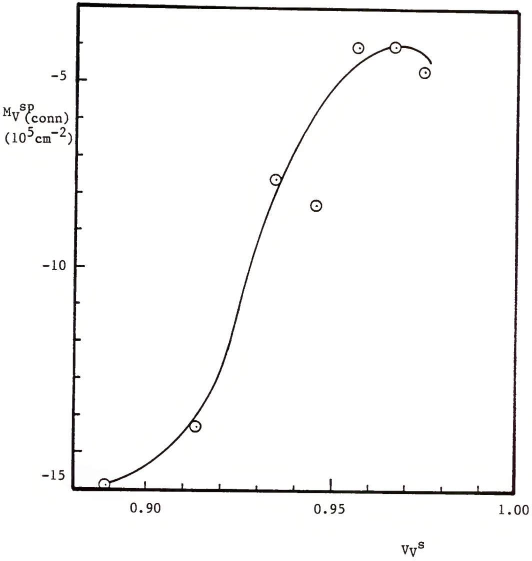

Figure 45. Dependence of integral mean curvature of the connected porosity on the volume fraction of solid during loose stack sintering of nickel at 1250°C.

along a cylindrical pore does not change the area of the boundary. On the other hand, simple equiaxed isolated pores may be expected to pin a grain boundary effectively. Presumably, the boundary remains pinned until the pore disappears by vacancy annihilation. However, as illustrated in Figure 43, there is an initial plateau of the volume fraction of isolated pores which suggests that at the beginning of the third stage there is a transient period for pore channels to disconnect and reach a lower limit of the volume fraction of connected pores. During this period pore channels disconnect to provide isolated pores which disappear such that the volume fraction of isolated pores maintains a plateau. This additional explanation does not conflict with the above rationalization.

The ratios, S_V^{conn}/S_V^{tot} and M_V^{conn}/M_V^{tot} were also determined on the area of the intermediate serial section (16th). These ratios were used to compute values of S_V^{conn} and M_V^{conn} corresponding to those on the calibrated surfaces by multiplying the ratios by the total values of S_V^{sp} and M_V^{sp} on the calibrated surfaces. These results are presented in Figures 44 and 45, respectively.

The path information obtained on a random uncalibrated section (6th section) during serial sectioning analysis are illustrated in Figure 60, in the form of a random test of the validity of the cell model on the entire field of sections of the samples, small portions of which were chosen for taking micrographs for the purpose of the serial sectioning analysis. This test is described in detail in the next chapter.

4.6 Kinematics

For the evaluation of the kinematics of microstructural evolution, it is necessary to determine the variations of the group one metric properties ($V_V{}^P$, $S_V{}^{sp}$ and $M_V{}^{sp}$) with sintering time together with topological properties ($\bar{N}_V$ - $\bar{G}_V$). Recall that these average velocities weighted differently:

$$\bar{v}_S \equiv \frac{1}{S_V^{sp}} \frac{dV_V^P}{dt} \tag{7}$$

$$\bar{v}_H \equiv \frac{1}{2M_V^{sp}} \frac{dS_V^{sp}}{dt} \tag{8}$$

$$\bar{v}_K \equiv \frac{1}{4\pi(N_V - G_V)} \frac{dM_V^{sp}}{dt} \tag{9}$$

The variations of the volume fraction of pore, pore-solid interface area per unit volume and integral mean curvature of pore-solid interface per unit volume with logarithms of time are presented in Figures 46, 47 and 48, respectively.

The plot of $V_V{}^P$(QM), $S_V{}^{sp}$ and $M_V{}^{sp}$ versus log t (t = time in sec) are described with reasonable precision by linear relation. The slopes of the lines fitted by the least square method are also presented in the Figure 46, 47 and 48.

The dependence of ($\bar{N}_V$ - $\bar{G}_V$) on the sintering time, i.e. the volume fraction of solid, was evaluated in Table 8.

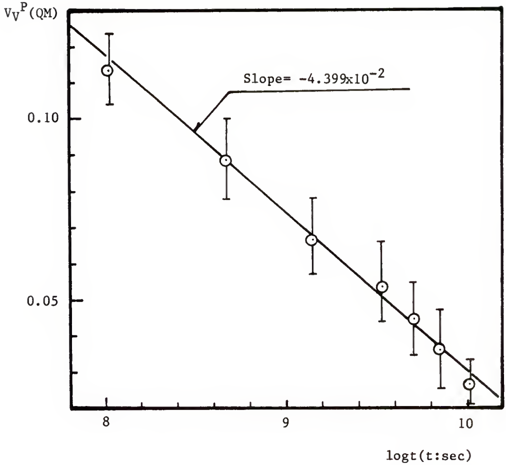

Figure 46. Dependence of volume fraction of pore (metallographic) on the logarithm of sintering time.

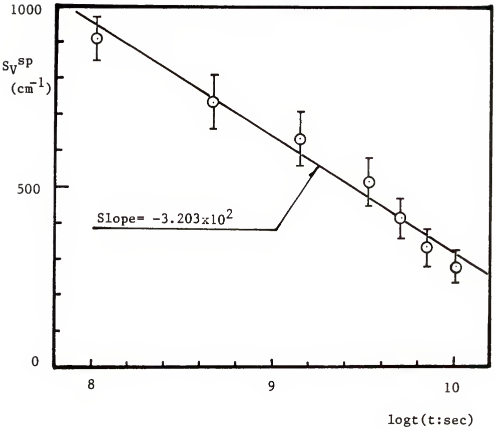

Figure 47. Dependence of surface area per unit volume on the logarithm of sintering time.

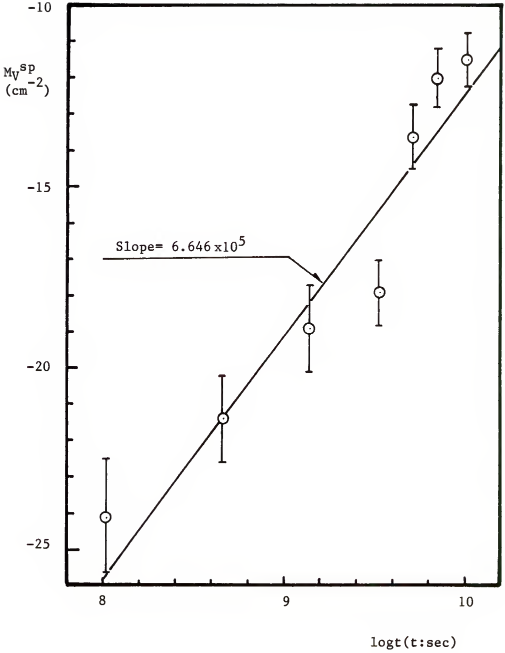

Figure 48. Dependence of integral mean curvature per unit volume on the logrithm of sintering time.

The three average interface velocities weighted differently [equations (7)-(9)] are evaluated in the next chapter. Distributions of these velocities are also discussed in the next chapter.

4.7 Kinetics

Images of the in-situ specimen during sintering at 1250°C are illustrated in Figure 49 at several sintering times. The in-situ changes in the diameter and the height of a cylindrical specimen were monitored by using a series of images of the specimen, as illustrated in Figure 49. The magnification of the sample in the images used for the acquisition of raw data was 2.593. Since acquisition of changes in diameter in this particular case gives a more correct value than that in height due to surface effect in images, the evaluation of density changes was based on the change of diameter.

The dependence of volume fraction of porosity on the sintering time is presented in Figure 50 for both a series of sintered samples (discontinuous sintering) and in-situ specimen (continuous sintering). The slopes of straight lines fitted by the least square method are shown in Figure 50. The general pattern of the two kinetic curves is identical; however, the slope of the straight line has a lower value for continuous sintering than for discontinuous sintering. This difference has its origins in two different histories of thermal path.

The slope of the straight line fitted in the range of time studied in this study, as illustrated in Figure 50, -3.085×10^{-2} was used for the purpose of evaluation of the densification rate. The measurements of density are presented in Table 9. The calculated densification rates tabulated in Table 11 are discussed in the next chapter.

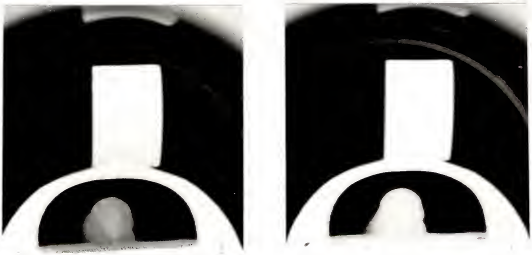

a) t= 9.0 min

b) t= 19.8 min

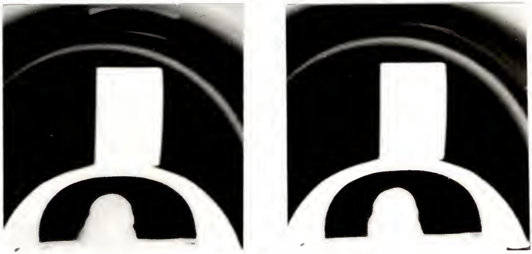

c) t= 76.4 min

d) t= 833.4 min

Figure 49. Photographs of in-situ specimen of 5.5 micron nickel powder during loose stack sintering at 1250°C at several sintering time.

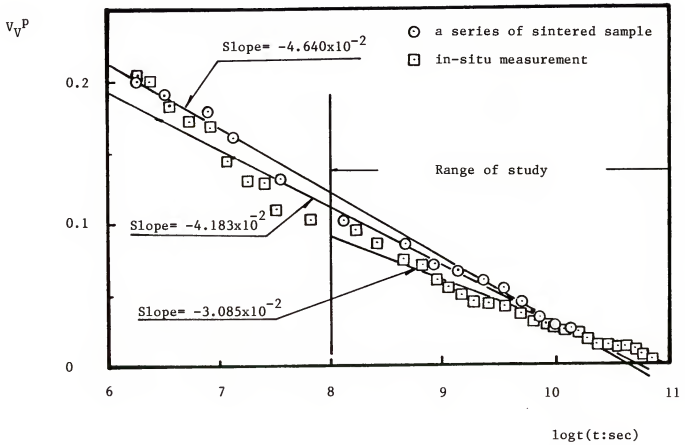

Figure 50. Dependences of volume fraction of pore on the logarithm of sintering time for a continuous sintering and a discontinuous sintering.

Table 9
Measurements of in-situ kinetics of INCO 123 nickel powder loose stack sintered at 1250°C

Sintering time(min)	V_V^s	V_V^P
56.4	0.902	0.098
76.4	0.923	0.077
98.5	0.925	0.075
113.4	0.929	0.071
128.4	0.942	0.058
143.4	0.946	0.054
163.4	0.951	0.049
183.4	0.955	0.045
208.4	0.958	0.042
233.4	0.960	0.040
263.4	0.964	0.036
293.4	0.966	0.034
323.4	0.968	0.032
358.4	0.970	0.030
393.4	0.973	0.027
433.4	0.975	0.025
473.4	0.981	0.019
518.4	0.982	0.018
563.4	0.983	0.017
613.4	0.985	0.015
663.4	0.986	0.014
713.4	0.987	0.013
773.4	0.991	0.009
833.4	0.993	0.007

The least square line; $V_V^P=0.338-3.085\times10^{-2}\log t$, where t in sec

CHAPTER 5
DISCUSSION

5.1 Introduction

Metal powders may be consolidated into useful products by a variety of processes. Practical processing generally involves cold pressing followed by sintering, or hot pressing under controlled conditions. Loose stack sintering, while not of general importance, provides a model process in which the microstructural evolution is driven by internal forces derived from the surface tension of the powder. Effects of external influence; e.g., applied stresses, upon the microstructural evolution, including its kinetics and final microstructural state, may be better understood by comparing their behavior to that exhibited in loose stack sintering.

The distribution of local interface velocities which describe the kinematics of the microstructural evolution of loose stack sintered powder will be discussed first. This discussion leads to a comparison of average vacancy concentration gradients during microstructural evolution of loose stack sintered powder evaluated from two independent considerations; i.e. 1) that computed from the cell model and the kinetics of the process, and 2) that estimated from capillarity theory and the thermodynamic of the system.

These discussions lead to a number of speculations about the direction of potential application of approach employed in this study to other sintering scenarios, including cold compaction and sintering, and hot pressing. Finally, the potential application of this approach to the intermediate stage of sintering in the loose stack sintered powders will be discussed.

5.2 Distribution of Local Interface Velocities

The characterization of growth (or shrinkage) during microstructural evolution can be couched in terms of the distribution of interface velocities in the system. Information about this distribution can be obtained from three average velocities, each with different weighting factors, as defined in equations (7)-(9); $\overline{v}_S$, the surface area averaged growth rate of the surface elements; $\overline{v}_H$, the curvature averaged growth rate; and $\overline{v}_K$, the growth rate averaged with respect to the spherical image. In sintering, $\overline{v}_S$ is represented by a negative velocity since the volume fraction of porosity decreases as densification proceeds. These three average interface velocities were plotted against the volume fraction of solid in Figure 51, and tabulated in Table 10.

The porosity consists of connected and isolated fractions in the range of densities studied in this investigation, as shown in Figure 43. The number of isolated pores which are formed at the end of the second stage by disintegrating the connected pores begins to increase toward a maximum value around 94% of volume fraction of solid, as shown in Figure 28. The disintegration of connected porosity continues to increase the number of isolated pores, which shrink and disappear in part as densification proceeds. After the maximum in the number of isolated pores is reached, only a few pores are isolated subsequently. From there on the isolated pores shrink and disappear. In contrast, the volume

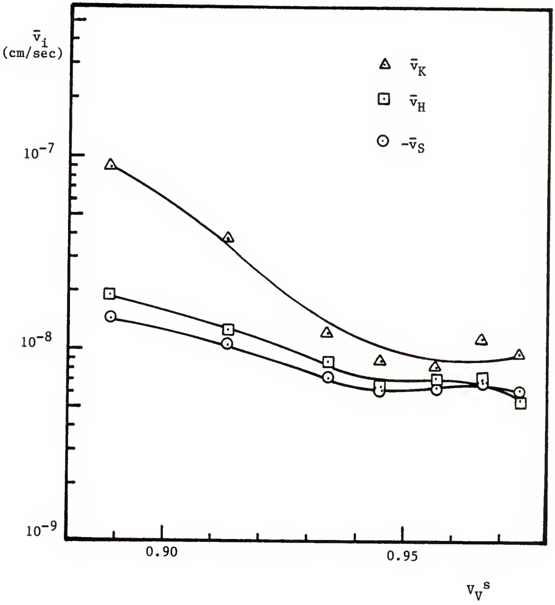

Figure 51. Comparison of surface average velocity, $\bar{v}_S$, mean curvature average velocity, $\bar{v}_H$, and Gaussian curvature average velocity, $\bar{v}_K$, during loose stack sintering 5.5 microns nickel powder at 1250°C.

Table 10
Kinematics of the microstructural evolution of
INCO 123 nickel powder loose stack sintered at 1250°C

t(min)	V_V^S(Arch)	dV_V^P/dt * $(10^{-5}sec^{-1})$	dS_V^{SP}/dt $(10^{-2}cm^{-1}sec^{-1})$	dM_V^{SP}/dt $(10^{2}cm^{-2}sec^{-1})$	$\bar{v}_S$ (**)	$\bar{v}_H$ (**)	$\bar{v}_K$ (**)
56.4	0.890	-1.300	-9.464	1.964	-1.424	1.961	9.055
97.4	0.914	-0.753	-5.481	1.137	-1.023	1.278	3.728
159.4	0.935	-0.460	-3.349	0.695	-0.729	0.884	1.240
231.4	0.946	-0.317	-2.306	0.479	-0.614	0.644	0.888
271.4	0.957	-0.270	-1.940	0.408	-0.650	0.714	0.822
316.4	0.968	-0.232	-1.687	0.350	-0.692	0.702	1.175
410.4	0.974	-0.179	-1.301	0.270	-0.631	0.561	0.989

* : Q.M.
** : 10^{-8}cm/sec

fraction of connected porosity changes only slightly. These observations has been described by a geometric model[19] in which the isolated pore takes an equiaxed geometry and the network pore a cylindrical geometry which has only three and one branch nodes. This description of behavior of porosity during sintering is contrasted to those models that involve only isolated porosity[42-45] or connected porosity.[42,46,47]

The distribution of the three average interface velocities shown in Figure 51 may be explained by a geometric kinematic model that is analogous to familiar nucleation and growth descriptions. Since, in the case of sintering, the volume fraction decreases with time, nucleation and growth models may be adapted by reversing the time axis. Accordingly, consider a site saturation growth model[27] in which the system consists of a fraction of particles growing spherically, (corresponding to shrinkage of isolated pores) and a fraction growing as rods (corresponding to disintegration of connected pores). If this growth rate in the radial direction and that in lengthwise direction are known, the three average interface velocities may be derived from these geometrical considerations.[27] Based on the observation that the change of volume fraction of connected porosity, as shown in Figure 43, it may be inferred that the rate of disconnection of connected porosity is very rapid up to 94% of volume fraction of solid and the decrease of the volume fraction of connected porosity is due solely to the disintegration of the network. The higher value of Gaussian curvature average velocity, $\overline{v}_K$, in this range of density, Figure 51, may be due to this high rate of disintegration (i.e. a high value of rate of shrinkage in the lengthwise direction) of connected pores. This argument may also be supported by the observation of the higher value of the rate of change of integral mean curvature with respect to sintering time, as shown in Table 10. As sintering enters the range of density in which the volume fraction of connected pores shows a plateau, the variation of $\bar{v}_K$ settles down to a constant level within some local fluctuations. This may be explained in terms of a saturated value in the rate of lengthwise shrinkage, therefore $\bar{v}_K$ in this range of density is due to the shrinkage and disappearance of isolated pores. In this respect, the rate of shrinkage in isolated pores may be thought to be constant. On the contrary, the other two average interface velocities, $\bar{v}_S$ and $\bar{v}_H$, exhibit approximately the same smooth decrease over the whole range of densities. This is due to the balanced decrease between the volume fraction of porosity and pore solid interface area with increase of volume fraction of solid. As shown in Figures 46 and 47, the slope of the straight line in the plot of volume fraction of pore versus log (sintering time) and pore solid interface area versus log (sintering time) may be said to be constant at each data point. This fact is also consistent with the smooth behavior of $\bar{v}_S$ and $\bar{v}_H$.

5.3 Vacancy Concentration Gradients

An expression for the average vacancy concentration gradients at pore-solid interface has been derived in Chapter 2, equation (42). An estimate of the same gradient may be obtained from thermodynamic consideration. The values of the average vacancy concentration gradients derived from these two considerations are evaluated and compared in this section.

5.3.1 Kinetic considerations

As described in Chapter 2, all of the parameters except the average vacancy concentration gradient are accessible through experiments, literature and inferences. The information sources used in computing this concentration gradient were summarized in Table 3.

5.3.1.1 The densification rate

The densification rate for the nickel powder under study was expressed in equation (39). The slope of the straight line obtained by the least squares method in the plot of volume fraction of pore versus log (sintering time), -3.085×10^{-2}, (see Figure 50) was used. A similar linear relationship between V_V^P and log (sintering time) was also obtained experimentally by Coble[48] in the late stage of sintering.

The evaluation and plot of densification rate in terms of change of pore volume per mole of solid with respect to sintering time versus volume fraction of solid are shown in Table 11 and Figure 52. Since pore volume decreases as densification proceeds, the densification rate has a negative sign. Although the path of microstructural evolution is not changed by a periodic thermal cycle of discontinuous heating and cooling,[37] the rate of change of the volume is sensitive to this choice of sintering scenarios. This is shown in Figure 50, where the change of volume fraction of porosity with respect to sintering time for a discontinuous process yielded a higher value of the slope than for a continuous (in-situ) process. In the latter case, the densification rate decreases rapidly initially and then smoothly with respect to volume fraction of solid as shown in Figure 52 and Table 11.

Table 11
Densification rate in terms of in-situ kinetics

Sintering time(min)	Densification rate $[10^{-5}cm^3/(mole.sec)]$
56.4	-6.014
97.4	-3.482
159.4	-2.128
231.4	-1.466
271.4	-1.250
316.4	-1.072
410.4	-0.826

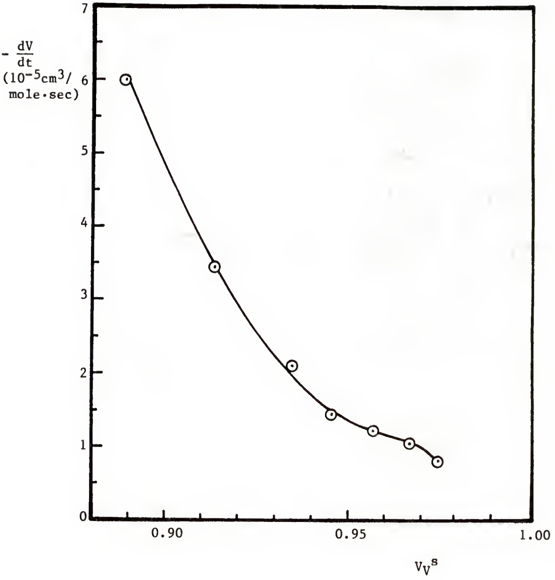

Figure 52. Densification rate in terms of a continous change of volume of pore per mole of nickel per sec versus volume fraction of solid for loose stack sintered 5.5 microns nickel powder at 1250°C.

5.3.1.2 The efficiency factor

The efficiency factor, defined as the ratio of the cell boundary area to the grain boundary area is essential in the conversion of the volume of vacancies annihilated at grain boundaries to the global volume of shrinkage of the system. The average efficiency factor, defined in equation (23), may be represented by the ratio of cell boundary area per unit volume to grain boundary area per unit volume in polycrystalline structure under the following assumptions; 1. all the cell faces have the same grain boundaries and 2. the distribution of vacancy annihilation rate of each face of a cell is narrow enough to be treated as an average quantity. Assumption 1 is evidently valid in the late stages of sintering where the grain boundary network is well formed. If the grain boundary network interacts randomly with the porosity, as shown in Chapter 2, this factor becomes the reciprocal of the volume fraction of solid which is equal to the value of $1/(1-V_V^P)$. However, there is a clear tendency for porosity to be associated with grain boundaries. As a conseqence, the efficiency factor and the reciprocal volume fraction of solid are expected to have different values. The efficiency factor is expected to be larger than the reciprocal of the volume fraction of solid. The two estimations of efficiency factor are tabulated in Table 12 and illustrated in Figure 53. The gap between these two quantities decreases and approaches zero as densification proceeds. An extrapolation of these curves in Figure 53 to $V_V^S=1$ will result in $\bar{f} = 1/(1-V_V^P) = 1$.

Table 12
Estimations of efficiency factor and y

V_V^s	$\bar{f}$		y (10^{-2})
	$1/(1-V_V^P)$	S_V^{cell}/S_V^{ss}	
0.890	1.124	1.248	7.082
0.914	1.095	1.237	6.094
0.935	1.070	1.123	4.431
0.946	1.058	1.105	4.715
0.957	1.045	1.100	4.870
0.968	1.034	1.091	5.808
0.974	1.027	1.064	4.129

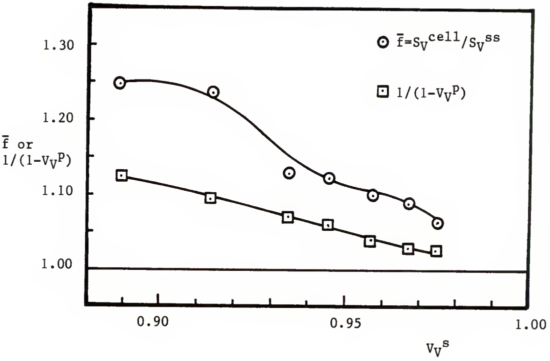

Figure 53. Variation of efficiency factor $\bar{f}$, and rough estimation of $\bar{f}[1/(1-V_V^P)]$ with volume fraction of the solid phase.

5.3.1.3 The parameter y

The dimensionless parameter y defined in equation (43) represents the relative dominance of grain boundary diffusion over volume diffusion of vacancies in the densification process. From the viewpoint of mass transport mechanisms in sintering, it is generally acknowledged[49] that volume diffusion and grain boundary diffusion only contribute to densification. No single theory[1-8] so far about sintering relates these two mechanisms to an equation or to one parameter which is contained in a densification rate equation. The cell model in this sense may be said to be a significant penetration of a fundamental problem in sintering. The evaluation of this parameter at this stage contains approximations which are described in Table 3. Consider the two approximations; 1. The ratio of the average vacancy concentration gradient over pore-solid interface area to that over ssp triple line is unity, and 2. The ratio of the grain boundary diffusivity to the volume diffusivity of vacancies is the same for atoms in the system. Assumption 1 is associated with the vacancy concentration over pore-solid interface, that over ssp triple line and the mean diffusion distance for vacancy annihilation which will be discussed later in this chapter. How the two parameters will be measured and vary with volume fraction of solid require much further study. However, it may be speculated that the average vacancy concentration over the pore-solid interface may be smaller than that near the ssp triple line, due to capillarity effects associated with the geometries. In contrast, the mean diffusion distance for a vacancy related with the pore solid interface will be larger than that for a vacancy associated with ssp triple line. These opposing effects make it likely that this ratio is within an order of magnitude of unity. Assumption 2 appears reasonable because the ratio of the two diffusivities may compensate for the differences in the activation energy and entropy terms in the pre-exponential between a vacancy and an atom in a polycrystalline structure. The other parameters, b, the thickness of enhanced diffusion zone, L_V^{ssp}, the length of ssp triple line per unit volume, and S_V^{sp}, pore solid interface area per unit volume, used to compute the parameter y, contain no ambiguities. Values of y based on the above analysis are represented in Table 12. The typical value of y ranges from 0.07 to 0.04, which means that the relative importance of grain boundary diffusion over volume diffusion at this temperature and stage of the process is not significant. Accordingly, volume diffusion is the dominant mechanism for a densification. The constants employed for evaluation of y are summarized in Table 13.

5.3.1.4 Average vacancy concentration gradient from kinetic considerations

All the information except D_V^{vac} in equation (43) are now available so that the average vacancy concentration gradient may be evaluated from the cell model. Considering the inferences described in 2.4.4.2 and information in Table 13, D_V^{vac} was evaluated to be:

$$D_V^{vac} \text{ in Ni} \simeq 1.11 \exp\left[\frac{-27.9(\text{kcal/mole})}{RT}\right](\text{cm}^2/\text{sec}) \qquad (49)$$

By inputting S_V^{sp}, L_V^{ssp} from Table 7, the densification rate, dV_V^p/dt from Table 11, the efficiency factor $\bar{f}$ from Table 12, $\Omega°$ from Table 13, y from Table 12, and D_V^{vac} in Ni [equation (49)] into equation (43), the kinetic average vacancy concentration gradient is evaluated, Table 15.

Table 13
Constants about nickel

Atomic weight[34] (gram/mole)	58.71
Density[34] (gram/cm^3)	8.902
Molar volume (cm^3/mole)	6.600
Atomic volume[34] (cm^3/atom)	1.09×10^{-23}
Surface energy[41] (ergs/cm^2)	2.28×10^{3}
Preexponential for self-diffusivity[29] (cm^2/sec)	1.11
Activation energy for self-diffusion[29] (kcal/mole)	64.9
Preexponential for grain boundary diffusivity[30] (bD°_b cm^3/sec)	4.358×10^{-10}
Activation energy for grain boundary diffusion[30] (kcal/mole)	28.2

The magnitude of this quantity ranges from -3.746 x 10^{18} vac/cm^4 to -1.866 x ^{18} vac/cm^4. Since the direction of vacancy diffusion fluxes is away from the source of vacancies; i.e. the pore-solid interface and near the ssp triple line, toward the sink of vacancy; i.e. the grain boundary, the sign of this gradient is negative. The large vacancy concentration gradient in the beginning of the late stage of sintering may be traced to a high densification rate as shown in Figure 52.

5.3.2 Thermodynamic considerations

The average vacancy concentration gradient may be obtained by applying the capillarity theory to a porous structure. A relation which describes the average vacancy concentration gradient in the porous sintered microstructure will be derived. Evaluation of this concentration gradient will follow.

5.3.2.1 The average vacancy concentration gradient from thermodynamic considerations

At any instant of observation a cell face may be visualized by Figure 54, in which considering the source of vacancy; i.e. pore-solid interface, ssp triple line, and the sink of vacancy, grain boundary, the thermodynamic average vacancy concentration gradient may be represented by

$$\langle \vec{\nabla} C_S \rangle_{\text{thermo}} \simeq \frac{\Delta C}{\bar{d}} \tag{50}$$

where ΔC represents the difference in vacancy concentration between the source and sink of vacancies and $\bar{d}$ is a mean diffusion distance for the

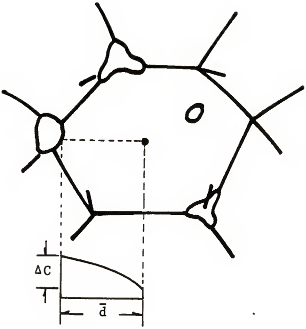

$$\langle \vec{\nabla} C_S \rangle_{\text{thermo}} = \frac{\Delta C}{\bar{d}}$$

Figure 54. Average vacancy concentration gradients by capillarity theory, where ΔC represents the differences in vacancy concentration between source and sink of vacancy, $\bar{d}$, mean diffusion distance for the annihilation of a vacancy.

annihilation of a vacancy. The vacancy concentration at the surface of pore-solid interface which has a mean curvature, $\bar{H}$ may be represented as

$$C_H^v = C_{H=0}^v\left(1+ \frac{2\gamma V^s}{RT}\bar{H}\right) \tag{51}$$

where $C_{H=0}^v$ represents the vacancy concentration in bulk material for which $H = 0$, γ is the surface energy, V^s is the molar volume, R, the gas constant, and T, the temperature (°K). Therefore,

$$\begin{aligned} \Delta C &= C_H^v - C_{H=0}^v \\ &= 2\, C_{H=0}^v \frac{\gamma V^s}{RT}\bar{H} \end{aligned} \tag{52}$$

5.3.2.2 The vacancy concentration of bulk material

No specific experimental information[50,51] exists about the equilibrium vacancy concentration in Ni. Therefore, an equilibrium vacancy concentration was inferred based on empirical rules[33] and experimental data.[50,51] The equilibrium vacancy concentration may be represented by

$$C_{H=0}^v = \left(\frac{\Delta N}{N}\right) \cdot \frac{1}{\Omega°} \tag{53}$$

where $\left(\frac{\Delta N}{N}\right)$ represents the fractional increase in the total number of of substitutional sites, $\Omega°$, the atomic volume (cm^3/atom). $\frac{\Delta N}{N}$ may be expressed as follows

$$\left(\frac{\Delta N}{N} \right) = \exp\left(\frac{\Delta S_v}{R} \right) \exp\left[\frac{-\Delta H_v}{RT} \right] \tag{54}$$

ΔS_V and ΔH_V represent the entropy change and the enthalpy change for the formation of vacancies in one mole of solid, respectively. From the empirical rules[33,50,51] for an FCC metal one may estimate $\Delta S_V \simeq 1.92R$. Similarly, an empirical rule for FCC metals permits estimation of the enthalpy of formation of a vacancy:

$$\Delta H_{v_{\text{in Ni}}} = 0.53\, Q_{SD}^{Ni} \; {}^{33,35} \tag{55}$$

where Q_{SD}^{Ni} is the activation energy for self diffusion of Ni. Based on the information in Table 13,

$$C_{H=0}^{v} \simeq 6.3 \times 10^{23} \exp\left[\frac{-37.0\ (\text{kcal/mole})}{RT} \right] (\text{vac/cm}^3) \tag{56}$$

5.3.2.3 The mean curvature of pore solid interface

The mean curvature of pore-solid interface defined in Figure 21 may be evaluated from the basic relationship[10]

$$\overline{H} \equiv \frac{M_V}{S_V} \tag{57}$$

Since the chemical potential near a curved surface, and the normal pressure acting upon a curved surface from surface tension is proportional to the local value of the mean curvature, this quantity may be a measure[10] of the average driving force in sintering under the action of surface tension.

This quantity may be divided into two contributions through serial sectioning analysis, since the volume fraction of pores may be divided into two parts, as shown in Figure 43; i.e. by isolated pores and by connected pores. The mean curvature of isolated pores increases rapidly but that of connected pore remains constant, as V_V^S increases as illustrated in Figure 55, and tabulated in Table 15. Since the mean curvature of connected pores does not vary as densification proceeds, the average vacancy concentration gradients associated with connected pores do not contribute to the vacancy diffusion flux for densification. Therefore, the mean curvature of isolated pore, $\bar{H}^{iso}$, may represent the effective mean curvature of the system for computing the densification rate. Based on this argument, the average concentration difference may be expressed as follows:

$$\Delta C_{eff.} = 2C^{v}_{H=0} \frac{\gamma V^{s}}{RT} \bar{H}^{iso} \tag{58}$$

5.3.2.4 Mean diffusion distance for the annihilation of a vacancy

The mean diffusion distance for the annihilation of a vacancy may be obtained from basic stereological relationships. This distance may be represented by $1/2(\bar{\lambda}^{ssp}_{g.b.})$, a half of the mean intercept between ssp triple line on the grain boundary, which is represented as follows

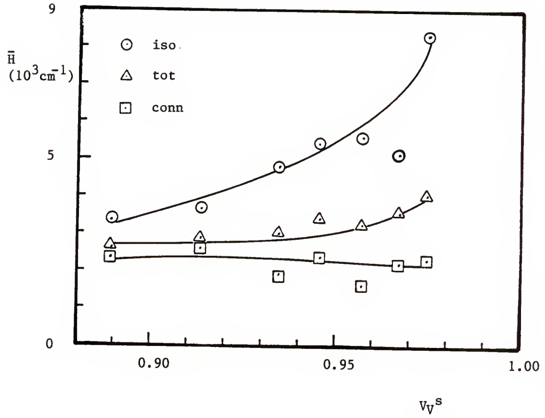

Figure 55. Variation of the mean curvature of isolated pores, connected pores and total pores with volume fraction of solid.

Table 14
Mean curvatures and mean diffusion distance for the annihilation of a vacancy

V_V^s	$\bar{H}(cm^{-1})$		$\bar{d}$ (micron)
	$\bar{H}$ tot	$\bar{H}$ eff*	
0.890	2643.45	3341.59	11.4
0.914	2913.06	3684.20	12.0
0.935	3002.74	4813.96	16.7
0.946	3469.87	5414.55	17.6
0.957	3267.42	5595.41	18.2
0.968	3582.25	5151.99	18.4
0.974	4092.12	8386.48	24.5

* $\bar{H}$ eff = $\bar{H}^{iso}$

$$\bar{d} \simeq \frac{1}{2}\,\bar{\lambda}^{ssp}_{g.b.}$$
$$= \frac{1}{2}\,\pi\,\frac{S_V^{ss}}{L_V^{ssp}} \tag{59}$$

The variation of the mean diffusion distance with volume fraction of solid is illustrated in Figure 56, and tabulated in Table 14. As densification proceeds, this distance increases.

5.3.2.5 Thermodynamic average vacancy concentration gradient

Thermodynamic average vacancy concentration gradient may be expressed as follows

$$\langle \nabla C_S \rangle_{\text{thermo}} = 2C^{V}_{H=0}\,\frac{\gamma V^{s}}{RT} \cdot \frac{\bar{H}^{iso}}{\bar{d}} \tag{60}$$

By inputting γ and V^s from Table 13, $\bar{H}^{iso}$ and $\bar{d}$ from Table 14, and $C^{V}_{H=0}$ at 1523°K from equation (56) into equation (60), the thermodynamic average vacancy concentration gradients are evaluated and tabulated in Table 15.

5.3.3 The comparison of average vacancy concentration gradients by two independent considerations

The evaluated values of a kinetic average vacancy concentration gradient and a thermodynamic average vacancy concentration gradient are tabulated and compared in Table 15, and plotted against volume fraction of solid in Figure 57. The ratio of kinetic gradient to thermodynamic

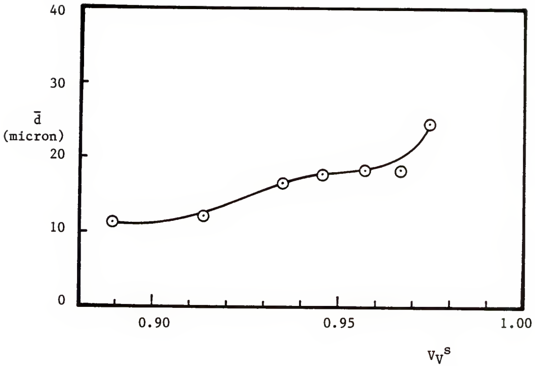

Figure 56. Variation of average diffusion distances for the annihilation of a vacancy ($\bar{d}=\frac{1}{2}\lambda_{g.b.}^{ssp}$) with the volume fraction of solid.

Table 15
Comparisons of average vacancy concentration gradients over pore-solid interfacial area

V_V^S	$<\vec{\nabla} C_S>$ (10^{18}vac/cm^4) kinetic	thermodynamic	Ratio kin/thermo
0.890	-3.746	-1.882	1.99
0.914	-2.739	-1.962	1.40
0.935	-2.186	-1.847	1.18
0.946	-1.866	-1.967	0.95
0.957	-1.980	-1.973	1.00
0.968	-2.105	-1.796	1.17
0.974	-2.002	-2.196	0.91

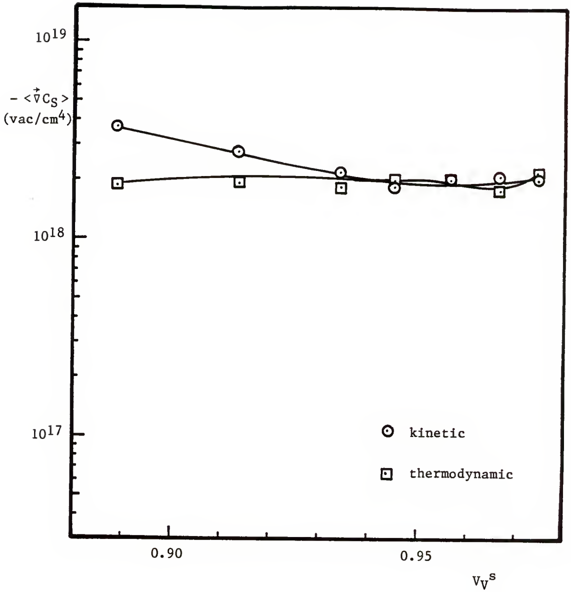

Figure 57. Comparison of variations of average vacancy concentration gradients over pore-solid interface area by kinetic considerations and those by thermodynamic considerations with the volume fraction of solid for 5.5 micron nickel powder loose stack sintered at 1250°C.

gradient ranges from 0.91 to 1.99. Considering the order of absolute value of vacancy concentration gradients, ~10^{18}, this agreement is very good. The thermodynamic gradient is insensitive to time whereas the kinetic gradient decreases as sintering proceeds.

5.4 Description of Behavior of Vacancy Annihilation

From equation (22) the average vacancy annihilation rate may be represented as follows:

$$\overline{\dot{n}}_A = \frac{dV}{dt}/-\Omega^\circ \overline{f} A_b \tag{61}$$

where A_b represents grain boundary area, which is the same quantity as S_V^{ss}. Since all the parameters on the right hand side of equation (61) are accessible through experiment and literature, $\overline{\dot{n}}_A$, the average vacancy annihilation rate may be evaluated; the results are tabulated in Table 16 and illustrated in Figure 58. It is interesting that the rate ranges from 4.3 x 10^{14} vac/cm^2 to 1.0 x 10^{15} vac/cm^2. As the volume fraction of solid increases, the vacancy annihilation rate decreases, as in Figure 58. The densification therefore may be explicitly described by use of the number of vacancy disappeared per unit area and unit time.

It may be interesting to evaluate the time, t, required for the annihilation of a mono-layer of vacancies. This is calculated by

$$t(\mathrm{sec}) = \frac{\mathrm{atom/cm^2}}{\overline{\dot{n}}(\mathrm{vac/cm^2 \cdot sec})} \tag{62}$$

Table 16
Behaviors of vacancy annihilation during sintering 5.5 micron nickel powders at 1250°C

V_V^s	$\bar{\dot{n}}$ $[10^{14}$ vac/(cm^2·sec)]	$\bar{t}$ (sec/monolayer)
0.890	10.382	1.55
0.914	8.270	1.95
0.935	6.447	2.50
0.946	4.901	3.29
0.957	4.896	3.30
0.968	4.354	3.70
0.974	4.303	3.74

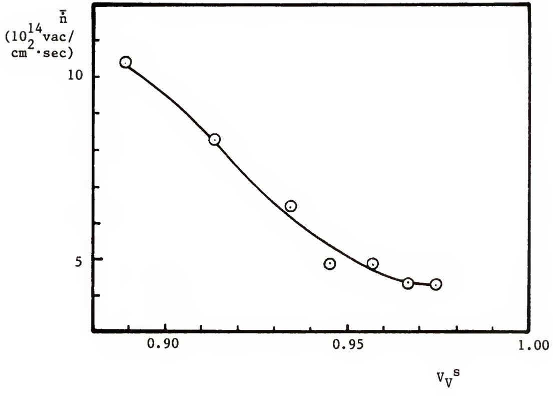

Figure 58. Dependence of average vacancy annihilation rate on the volume fraction of solid for 5.5 micron nickel powder loose stack sintered at 1250°C.

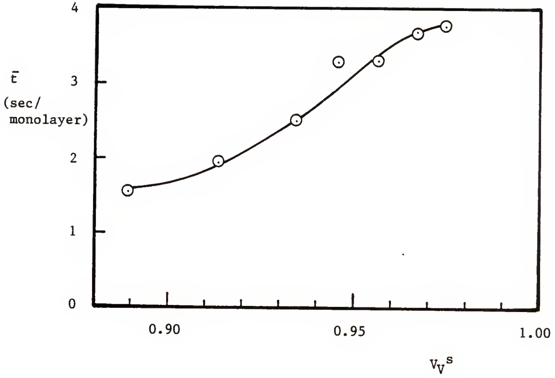

Figure 59. Variations of average time required for a monolayer of vacancy to annihilate with volume fraction of solid for 5.5 micron nickel powder loose stack sintered at 1250°C.

Figure 59 represents the dependence of the average time required for a monolayer of vacancies to be annihilated upon the volume fraction of solid. As densification proceeds, the time for annihilation increases. This is due to an increase in the mean diffusion distance for vacancy annihilation, as shown in Figure 56.

5.5 Generality of the Cell Model and Speculations for Further Studies

In deriving the cell model, the densification rate equation,

$$\frac{dV_V^P}{dt} = \Omega^\circ \ \bar{f} D_V^{vac} \langle \nabla C_S \rangle \ S_V^{sp}(1+y) = -\Omega^\circ \bar{f} \ \bar{\dot{n}} \ A_b$$

the only geometric assumption used was that the grain boundaries are planar. This is not an important assumption in sintering. Therefore, the cell model may be said to be geometrically general.

Since this model is based on the process in which no external influence is applied, some modifications will be required in order to apply it to other sintering scenarios which are commercially important, including cold pressing and sintering, and hot pressing.

The test of cell model described in this study was over the range of $V_V^S = 0.890 - 0.974$, i.e. in the late stage of sintering. Therefore, it is interesting to speculate about the application of the cell model to the intermediate stage of sintering.

5.5.1 A test on an intermediate section of the specimen during serial sectioning analysis

The path of metric properties was measured on an intermediate section, i.e. the 6th section of the specimen, which had not been calibrated. A repetition of all procedures described above for the evaluation and comparison of the kinetic average vacancy concentration gradients and the thermodynamic average vacancy concentration gradients is shown in Figure 60. The same comparison in Figure 57 for the calibrated surfaces may be compared with that in Figure 60 for the uncalibrated surfaces. No significant differences may be found between them. Based on these observations it may be safe to say that the kinetic theory, i.e. the cell model has a general applicability in any place inside the sample as long as the statistics employed in order to measure the stereological parameters are reasonably maintained.

5.5.2 Cold pressing and sintering in the late stages of sintering

The characterization of metric properties, as shown in Table 17, has been done on INCO 123 nickel powder cold pressed under the pressure of 25000 psi and sintered at 1250°C in H_2.[22] The application of the model to this sintering scenario had been expected to show a good agreement with that shown in the loose stack sintering once the plastic deformation which might have been involved during cold compaction has been annealed out so that there remains no driving force for sintering in addition to surface tension.

The results of this analysis, shown in Table 18 and illustrated in Figure 61, demonstrate that the thermodynamic gradient is larger than the kinetic gradient. An interpretation of this gap may require further

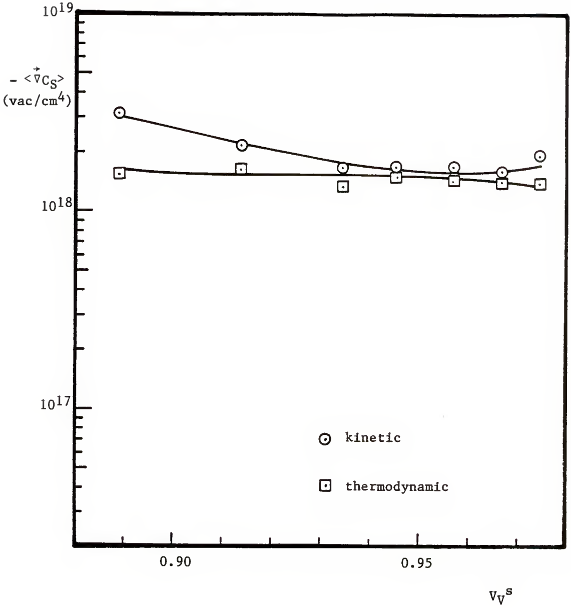

Figure 60. Comparison of variations of average vacancy concentration gradients over pore-solid interface area by two independent considerations with the volume fraction of solid at a random section (no.6 section) during the serial sectioning analysis of 5.5 micron nickel powder loose stack sintered at 1250°C.

Table 17

Data for analysis of the general kinetic theory for INCO 123 nickel powder cold pressed (25000psi) and sintered at 1250°C in H_2[22]

Sintering time(min)	10	30	150	1200
V_V^s	0.927	0.955	0.969	0.990
dV^P/dt^* $(10^{-4}cm^3/mole.sec)$	-1.356	-0.452	-0.090	-0.011
$S_V^{sp}(cm^{-1})$	1230.0 ±137.0	646.7 ±63.6	444.2 ±52.1	140.0 ±23.2
$M_V^{sp}(-10^5cm^{-2})$	60.79 ±2.80	39.24 ±1.16	21.99 ±1.43	6.12 ±0.51
$S_V^{ss}(cm^{-1})$	448	384	328	149
$\bar{f}(\frac{S_V^{cell}}{S_V^{ss}})$	1.732	1.606	1.136	1.001
$L_V^{ssp}(10^5cm^{-2})$	11.796	6.777	2.870	0.372

* $V_V^P = 0.145-1.233\times10^{-2}\log t\,(t:sec)$

Table 18
The results of analysis of the general kinetic theory for INCO 123 nickel powder cold pressed (25000psi) and sintered at 1250°C in H_2

$V_V{}^s$		0.927	0.955	0.969	0.990
$y\,(10^{-2}cm^0)$		6.96	7.61	4.69	1.93
$\bar{H}\,(10^3cm^{-1})$		4.942	6.068	4.951	4.371
$\bar{d}\,(10^{-4}cm)$		6.0	8.9	18.0	62.9
$<\vec{\nabla}C_S>$	kinetic	-4.524	-3.074	-1.301	-0.601
$(10^{18}vac/cm^4)$	thermo	-5.307	-4.367	-1.767	-0.445
Ratio kinetic/thermo		0.85	0.70	0.74	1.35
$\bar{\dot{n}}\,(10^{14}vac/cm^2.sec)$		24.300	10.192	3.374	1.054
$\bar{t}$(sec/monolayer)		0.66	1.58	4.78	15.31

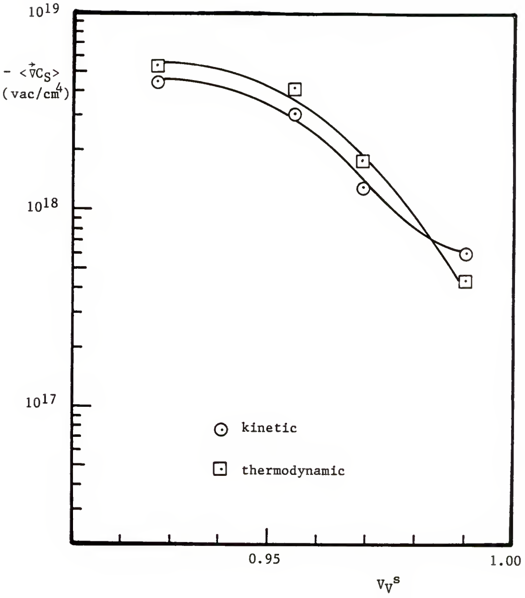

Figure 61. Comparison of variations of average vacancy concentration gradients over pore solid interface by two independent considerations with the volume fraction of solid for 5.5 micron nickel powder cold pressed (25000 psi) and sintered at 1250°C in H_2.

study. However, the good agreement between these two gradients may indicate that the external influences are not important at the stage of sintering represented.

5.5.3 Hot pressing in the late stage of sintering

The metric properties of hot pressed INCO 123 nickel powder has been characterized,[19] as shown in Table 19. During hot pressing heat and pressure are applied simultaneously. Thus, driving forces besides surface tension are added due to applied pressure. Therefore, a higher value of densification rate is expected such that the kinetic average vacancy concentration gradients show a higher value than the thermodynamic gradient.

The results of this analysis of kinetic theory are shown in Table 20 and illustrated in Figure 62. The value of the kinetic gradients is approximately twice that of thermodynamic gradients. What fraction of applied pressure has been transferred as a driving force for densification remains to be studied.

A short time for the annihilation of one layer of vacancy in $1cm^2$ in Table 20 may represent another aspect of high densification rate which is assisted by external additional driving force for densification.

5.5.4 Loose stack sintering in the intermediate stage of sintering

The cell model does not contain any significant geometric assumptions, therefore the cell model may also be applied to the intermediate stage of sintering.

Table 19

Data for analysis of the general kinetic theory for INCO 123 nickel powder hot pressed (2000 psi) at 1250°C in vacuum[19]

Sintering time(min)	8	16	22	40	150
$V_V{}^s$	0.930	0.943	0.958	0.968	0.984
dV^P/dt^* $(10^{-4}cm^3/mole.sec)$	-2.551	-1.276	-0.928	-0.510	-0.136
$S_V{}^{sp}(cm^{-1})$	774.32 ±105.0	561.48 ±87.0	425.12 ±56.0	360.24 ±62.0	284.46 ±48.0
$M_V{}^{sp}\,(-10^5cm^{-2})$	49.67 ±1.80	32.99 ±3.10	28.33 ±1.80	22.99 ±2.70	14.45 ±1.90
$S_V{}^{ss}(cm^{-1})$	570.1 ±47.0	537.3 ±38.0	422.2 ±39.0	303.0 ±25.0	164.4 ±22.0
$\bar{f}\left(\frac{S_V{}^{cell}}{S_V{}^{ss}}\right)^{**}$	1.80	1.65	1.50	1.40	1.12
$L_V{}^{ssp}\,(10^6cm^{-2})$	1.202	0.719	0.404	0.266	0.127

* $V_V{}^P = 0.181 - 1.856\text{x}10^{-2}\log t\,(t\text{:sec})$

** Estimated

Table 20
The results of analysis of the general kinetic theory for INCO 123 nickel powder hot pressed (2000 psi) at 1250°C in vacuum

V_V^S		0.930	0.943	0.958	0.968	0.984
y $(10^{-2}cm^0)$		11.270	9.290	6.894	5.359	3.240
$\bar{H}$ $(10^3 cm^{-1})$		6.415	5.876	6.664	6.382	5.080
$\bar{d}$ $(10^{-4}cm)$		7.5	11.7	16.4	17.9	20.3
$<\vec{V}_{C_S}>$ $(10^{18}$ vac/cm$^4)$	kinetic	-12.502	-9.575	-10.343	-7.298	-3.144
	thermo	-5.515	-3.205	-2.600	-2.285	-1.600
Ratio kinetic/thermo		2.27	2.99	3.98	3.19	1.96
$\bar{\dot{n}}$ $(10^{14}$ vac/cm^2.sec)		34.561	20.003	20.368	16.722	10.275
$\bar{t}$(sec/monolayer)		0.47	0.81	0.79	0.96	1.75

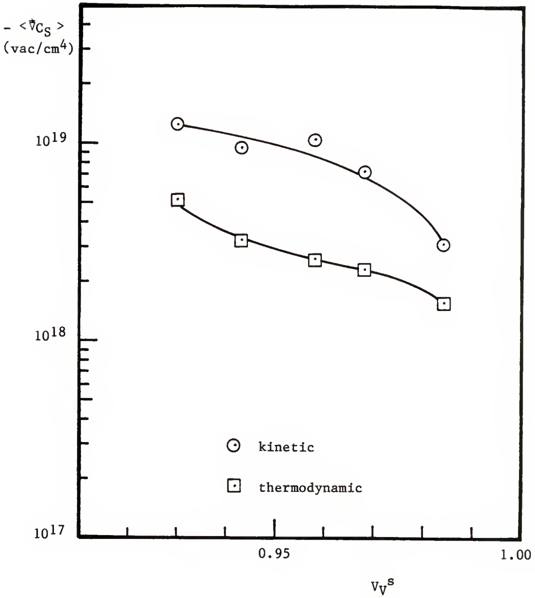

Figure 62. Comparison of variations of average vacancy concentration gradients over pore solid interface by two independent considerations with the volume fraction of solid for 5.5 micron nickel powder hot pressed (2000 psi) at 1250°C in vacuum.

The metric properties of 48 micron pure LINDE spherical copper powder loose stack sintered at 1000°C under H_2 has been characterized,[21,29] as shown in Table 21.

By employing the procedure described in 2.4.4.2 together with appropriate information in Table 22, D_V^{vac} in Cu was inferred as follows

$$D_V^{vac} \text{ in Cu} \approx 0.33 \exp[\frac{-20.7(\text{kcal/mole})}{RT}](\text{cm}^2/\text{sec}) \qquad (63)$$

By applying the procedure described in 5.3.2.2 together with appropriate information in Table 22,

$$C_{H=0}^{v} \text{ in Cu} \approx 3.8 \times 10^{23} \exp[\frac{-27.5(\text{kcal/mole})}{RT}](\text{vac/cm}^3) \qquad (64)$$

where $\Delta S_v = 1.5R$ for copper[35] was used.

Repetition of the procedure employed for the analysis of the general kinetic theory in Ni by using information in Tables 21 and 22 together with Equations (63) and (64) yielded the results for Cu, Table 23. The results of the analysis are illustrated in Figure 63.

The general patterns of the variations of vacancy concentration gradients with proceeding of densification are characterized by; 1) A smooth decrease of kinetic vacancy concentration gradients and 2) A change in the direction of thermodynamic vacancy concentration gradients at the initial stage of sintering and little change thereafter. A complete interpretation of these behaviors needs further studies including 1) precise measurements of sintering kinetics, 2) measurements of metric properties including cell boundary area and length of ssp

Table 21
Data for analysis of the general kinetic theory for 48 micron pure LINDE spherical copper powder loose stack sintered at 1000°C in H_2[21,52]

Sintering time (hours)	2	3	8	16	32	64	127	510
$V_V{}^S$	0.668	0.734	0.770	0.784	0.799	0.843	0.848	0.863
dV^P/dt^* ($10^{-6}cm^3$/mole.sec)	-31.2	-20.5	-7.8	-3.9	-2.0	-1.0	-0.5	-0.1
$S_V{}^{SP}$ (cm^{-1})	520	460	362	356	330	250	226	218
$M_V{}^{SP}$ ($10^5 cm^{-2}$)	1.41	-3.09	-3.42	-3.60	-3.34	-2.97	-2.48	-2.82
$S_V{}^{SS}$ (cm^{-1})	50	140	170	210	240	250	230	220
$\bar{f}^{**}$ ($S_V{}^{cell}/S_V{}^{SS}$)	8.3	4.8	3.3	3.3	3.3	2.6	2.6	1.7
$L_V{}^{SSP**}$ ($10^5 cm^{-2}$)	1.71	2.84	2.75	2.73	2.50	1.49	1.30	0.80

* $V_V{}^P = -0.032 \ln t + 0.312$ (t:hours)
** estimated

Table 22
Constants about copper

Atomic weight[34] (gram/mole)	63.54
Density[34] (gram/cm^3)	8.9
Molar volume (cm^3/mole)	7.139
Atomic volume[34] (cm^3/atom)	$1.18x10^{-23}$
Surface energy[41] (ergs/cm^2)	$1.72x10^3$
Preexponential for self-diffusivity[53] (cm^2/sec)	0.33
Activation energy for self-diffusion[53] (kcal/mole)	48.2
Preexponential for grain boundary diffusivity[49] ($bD°_b$ cm^3/sec)	$5.12x10^{-9}$
Activation energy for grain boundary diffusion[49] (kcal/mole)	25.12

Table 23
The results of analysis of the general kinetic theory for 48 micron pure LINDE spherical copper powder loose stack sintered at 1000°C in H_2

V_V^s		0.668	0.734	0.770	0.784	0.799	0.843	0.848	0.863
y ($10^{-2}cm^0$)		4.87	9.17	11.25	11.40	11.22	8.62	8.65	5.49
$\bar{H}$ (cm^{-1})		-271.2	671.7	944.8	1011.2	1012.1	1188.0	1097.4	1293.6
$\bar{d}$ ($10^{-4}cm$)		4.2	7.1	9.0	11.1	13.9	24.3	25.7	39.5
$<\vec{\nabla}C_S>$	kinetic	-8.97	-11.07	-7.64	-3.88	-2.15	-1.60	-0.89	-0.28
(10^{17} vac/cm^4)	thermo	9.97	-14.67	-16.42	-14.17	-11.32	-7.61	-6.66	-5.10
Ratio kinetic/thermo		-0.90	0.75	0.47	0.27	0.19	0.21	0.13	0.05
$\bar{\dot{n}}$ (10^{13} vac/cm^2.sec)		74.07	28.97	13.62	5.51	2.47	1.58	0.86	0.27
$\bar{t}$ (sec/monolayer)		2.06	5.27	11.21	27.69	61.70	96.41	177.39	565.58

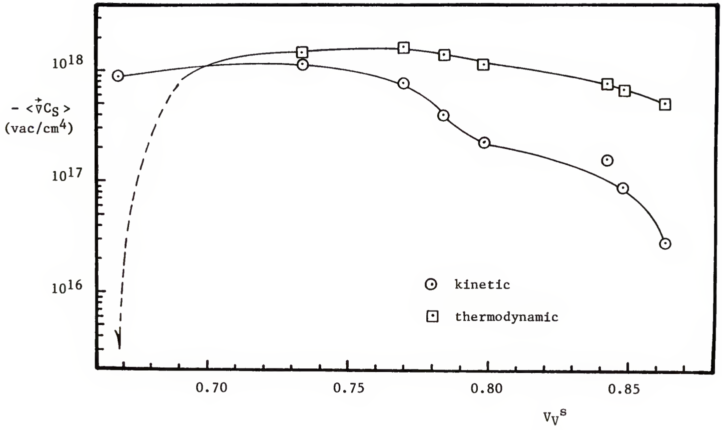

Figure 63. Comparison of variation of average vacancy concentration gradients over pore solid interface by two independent considerations with the volume fraction of solid for 48 micron pure LINDE spherical copper powder loose stack sintered at 1000°C under H_2.

triple lines, and 3) measurements of effective mean curvature, $H_{eff.}$ through serial sectioning analysis.

The findings of this investigation are summarized and courses of future research are suggested in the next chapter.

CHAPTER 6
CONCLUSIONS

6.1 Introduction

The discussion of the results of this investigation is summarized; an outline of suggested research is also presented.

6.2 Conclusions

1) It was confirmed that it is the isolated pores that disappear and connected pores remain in loose stack sintering over the range of 89% through 97% of volume fraction of solid.

2) The densification rate, in terms of the change of volume fraction of pores with respect to sintering time, was influenced by a thermal cycle of heating and cooling during sintering which, however, does not change the path of microstructural evolution.

3) The value of the average interface velocities over the spherical image was the highest and then was followed in magnitude by that averaged over mean curvature and that over the pore surface.

4) The mean curvature of pore-solid interface may be divided into two parts; i.e. isolated pores and connected pores. It was found that the mean curvature of connected pores does not contribute to the vacancy diffusion flux for densification. That of isolated pores may represent the effective mean curvature of the system for densification.

5) The efficiency factor may be used as an indicator for the degree of association of porosity with grain boundaries during the sintering process. A larger value of the efficiency factor represents a larger association of porosity with grain boundaries.

6) The kinetic average vacancy concentration gradients and thermodynamic concentration gradients agreed very well with each other for the late stage of loose stack sintering. This suggests that the cell model has an important and sufficient experimental background.

7) The cell model has a potential applicability to other sintering scenarios including cold pressing and sintering, hot pressing, and loose stack sintering in the intermediate stage of sintering.

8) The y parameter employed in the cell model contains a very important meaning which combines two mass transport mechanisms for densification into one parameter. The value of y represents the relative importance of grain boundary diffusion over volume diffusion.

9) The grain boundary diffusion plays only a minor role in the late stage of loose stack sintering of Ni at around 0.9 of homologous temperature (T/Tm); volume diffusion is the dominant transport mechanism according to the cell model.

10) The rate of vacancy annihilation was very rapid initially and decreases to a certain value in the late stage of loose stack sintering.

6.3 Suggestions for Further Study

In order to expand and confirm the applicability of the cell model which has been examined in this study, the following course of research is outlined.

1) Measurement of the sintering force during cold pressing and sintering and hot pressing may provide the information about the amount of plastic deformation which influences the behavior of densification.

2) Stress analysis by a systematic analytical method during cold pressing and sintering and hot pressing may provide a basis for the analysis of external influences which may affect the densification behavior.

3) Application of the cell model on the effects of environmental gas during sintering, including inert gas, may provide an insight about the role of the gas during sintering.

4) A systematic analysis of the distribution of vacancy concentration around sources and sinks for vacancy during densification will enhance the understanding of the details of sintering.

5) A rationalization of the rate of disintegration of a pore network will provide a basis for a model analysis of the distribution of interface velocities during loose stack sintering.

6) Measurement of precise kinetics together with metric properties and topological properties for the intermediate stage of sintering will expand the applicability of the general kinetic theory.

REFERENCES

1. J. Frenkel, J. Phys., (USSR) 9(5), 385 (1945).

2. G. C. Kuczynski, Trans. AIME, 185, 169 (1949).

3. W. D. Kingery and M. Berg, J. Appl. Phys., 26, 1250 (1955).

4. C. Herring, J. Appl. Phys., 21, 301 (1950).

5. B. Alexander and R. Balluffi, Acta Met., 5, 666 (1957).

6. R. Coble, J. Am. Ceram. Soc., 41, 55 (1958).

7. D. L. Johnson and T. M. Clark, Acta Met., 12, 1173 (1964).

8. J. G. Early, F. V. Lenel and G. S. Ansell, Trans. AIME, 230, 1641 (1964).

9. F. N. Rhines, Plansee Proceedings, 3rd Seminar, Reutte, Troyl, 38 (1958).

10. F. N. Rhines, R. T. DeHoff and J. Kronsbein, Final report to U.S. Atomic Energy Commission, Contract No. AT-(40-1)-2581, 40 (1969).

11. R. T. DeHoff, Metallography 8, 71 (1975).

12. R. T. DeHoff, Treatise on Materials Science and Technology, 1, 247 (1972).

13. R. T. DeHoff and F. N. Rhines, "A Topological Study of the Sintering Process," ACE Contract No. AT-(40-1)-2581, Annual Report (1968) Appendix II.

14. R. T. DeHoff, Science of Sintering, 16, 97 (1984).

15. R. T. DeHoff, E. H. Aigeltinger and K. R. Craig, J. of Microscopy, 95(1), 69 (1972).

16. L. K. Barrett and C. S. Yust, Trans. AIME, 239, 1172 (1967).

17. J. W. Cahn, Acta Met., 14, 477 (1967).

18. R. T. DeHoff, in Practical Applications of Quantitative Metallography, ASTM STP 839, 146 (1984).

19. A. S. Watwe, Doctoral Dissertation, University of Florida (1983).

20. S. D. Vora, Master's Thesis, University of Florida (1984).

21. E. H. Aigeltinger, Doctoral Dissertation, University of Florida (1969).

22. G. Q. Liu, Unpublished Research, University of Florida (1984).

23. R. T. DeHoff, Acta Met., 32(1), 43 (1984).

24. R. T. DeHoff, in Sintering and Heterogeneous Catalysis, Materials Science Research, 16, Plenum, New York, 23 (1984).

25. R. T. DeHoff, Metals Forum, 5(1), 4 (1982).

26. R. T. DeHoff, Private Communication (1986).

27. A. M. Gokhale, C. V. Iswaran, and R. T. DeHoff, Met. Trans., 10A, 1239 (1979).

28. Metal Powder Association Standard 4-45 (1945).

29. A. Hässner and W. Lange, Phys. Status Solidi, 8, 77 (1965).

30. W. Lange, A. Hässner and G. Mischer, Phys. Status Solidi, 5, 63 (1964).

31. R. E. Hoffman, F. W. Pikus, R. A. Ward, Trans. AIME J. of Met., 206, 483 (1956).

32. D. F. Kalinovich, I. I. Kovenskii, and M. D. Smolin, Fiz. Tverd. Tela, 10(2), 569 (1968).

33. A. M. Brown and M. F. Ashby, Acta Met., 28, 1085 (1980).

34. R. C. Weast, CRC Handbook of Chemistry and Physics, 66th Edition, CRC Press, Inc., Boca Raton, Fl. (1986).

35. P. G. Shewmon, Diffusion in Solids, 74, McGraw-Hill, New York (1963).

36. International Nickel Company [INCO] pamphlet, 5M-5498, INCO, New York (1975).

37. F. Thümmler and N. Thomma, Met. Review, 12, 69 (1967).

38. R. T. DeHoff and F. N. Rhines, eds., Quantitative Microscopy, McGraw-Hill Book Co., New York (1967).

39. R. E. Reed-Hill, Physical Metallurgy Principles, 2nd Edition, 311-637, D. Nostrand Company, New York (1973).

40. D. A. Porter and K. E. Easterling, Phase Transformations in Metals and Alloys, 116-142, Van Nostrand Reinhold (U.K.) Co., Ltd., Berkshire, England (1981).

41. L. E. Murr, Interfacial Phenomena in Metals and Alloys, Addison-Wesley, Reading, Mass. (1975).

42. R. L. Coble, J. Appl. Physics, 32, 787 (1961).

43. G. C. Kuczynski, Acta Met., 4, 58 (1956).

44. A. R. Hingorany and J. S. Hirschhorn, Intl. J. Powder Met., 2, 5 (1966).

45. A. J. Markworth, Scripta Met., 6, 957 (1972).

46. R. A. Gregg and F. N. Rhines, Met. Trans., 4, 1365 (1973).

47. G. C. Kuczynski, Sintering and Related Phenomena, 325, Plenum Press, New York (1976).

48. R. L. Coble, J. Appl. Physics, 32, 793 (1961).

49. F. B. Swinkels and M. F. Ashby, Acta Met., 29, 259 (1981).

50. R. O. Simmons and R. W. Balluffi, Phys. Rev., 117, 52 (1960).

51. R. O. Simmons and R. W. Balluffi, Phys. Rev., 125, 862 (1962).

52. R. A. Gregg, Doctoral Dissertation, University of Florida (1968).

53. K. Monma, H. Suto, and Oikawa, J. Japan Inst. Metals, 28, 188, (1964).

BIOGRAPHICAL SKETCH

SUN-MOO HER was born on January 10, 1951, in Kyoung-Ki Do, Republic of Korea. He has two children, Jin-Sun and Seung-Bum with Hoon-Ja Park HER.

In February, 1973, he received his B. S. in metallurgical engineering from Seoul National University (S.N.U.), Seoul, Korea.

Since then, after four months of military training, he has been an army officer of science and technology, a research engineer and a senior research engineer in Hong-Neung Machinery Co., Seoul, Korea.

He finished his M.S. in metallurgical engineering from S.N.U. as a recipient of a full scholarship from Hong-Neung Machinery Co. from March, 1979, to February, 1981. In January, 1984, he joined the Department of Materials Science and Engineering, University of Florida, Gainesville, Florida, as a Ph.D. graduate student, on leave from Hong-Neung Machinery Co.

He is a recipient of several awards including an award from the president of Hong-Neung Machinery Co. and two awards from the defense secretary of Korea.

He is a member of the Korean Institute of Metals and a joint student member of the American Society for Metals and the Metallurgical Society of AIME. He is also a fellow member of Tau Beta Pi and Alpha Sigma Mu.

I certify that I have read this study and that in my opinion it conforms to acceptable standards of scholarly presentation and is fully adequate, in scope and quality, as a dissertation for the degree of Doctor of Philosophy.

R T DeHoff

R. T. DeHoff, Chairman
Professor of Materials Science
and Engineering

I certify that I have read this study and that in my opinion it conforms to acceptable standards of scholarly presentation and is fully adequate, in scope and quality, as a dissertation for the degree of Doctor of Philosophy.

G. J. Abbaschian
Professor of Materials Science
and Engineering

I certify that I have read this study and that in my opinion it conforms to acceptable standards of scholarly presentation and is fully adequate, in scope and quality, as a dissertation for the degree of Doctor of Philosophy.

E D Whitney

E. D. Whitney
Professor of Materials Science
and Engineering

I certify that I have read this study and that in my opinion it conforms to acceptable standards of scholarly presentation and is fully adequate, in scope and quality, as a dissertation for the degree of Doctor of Philosophy.

R.W. Gould

R. W. Gould
Professor of Materials Science
and Engineering

I certify that I have read this study and that in my opinion it conforms to acceptable standards of scholarly presentation and is fully adequate, in scope and quality, as a dissertation for the degree of Doctor of Philosophy.

R. L. Scheaffer
Professor of Statistics

This dissertation was submitted to the Graduate Faculty of the College of Engineering and to the Graduate School and was accepted as partial fulfillment of the requirements for the degree of Doctor of Philosophy.

December 1986

Dean, College of Engineering

Dean, Graduate School